Bioinspired Design of a Landing System with Soft Shock Absorbers for Autonomous Aerial Robots

Ketao Zhang[1], Pisak Chermprayong[1], Dimos Tzoumanikas[2], Wenbin Li[2], Marius Grimm[2], Mariusz Smentoch[1], Stefan Leutenegger[2] and Mirko Kovac[1]

[1]Aerial Robotics Lab, Department of Aeronautics, Imperial College London, UK

[2]Department of Computing, Imperial College London, UK

{ketao.zhang, pisak.chermprayong10, dimosthenis.tzoumanikas14, wenbin.li, marius.grimm17}@imperial.ac.uk

smentochm@gmail.com, {s.leutenegger, m.kovac}@imperial.ac.uk

Abstract

One of the main challenges for autonomous aerial robots is to land safely on a target position on varied surface structures in real world applications. Most of current aerial robots (especially multirotors) use only rigid landing gears, which limit the adaptability to environments and can cause damage to the sensitive cameras and other electronics onboard. This paper presents a bioinpsired landing system for autonomous aerial robots, built on the inspire-abstract-implement design paradigm and an additive manufacturing process for soft thermoplastic materials. This novel landing system consists of 3D printable Sarrus shock absorbers and soft landing pads which are integrated with an 1-DOF actuation mechanism. Both designs of the Sarrus shock absorber and the soft landing pad are analysed via Finite Element Analysis (FEA), and are characterized with dynamic mechanical measurements. The landing system with 3D printed soft components is characterized by completing landing tests on flat, convex and concave steel structures and grassy field in a total of 60 times at different speeds between 1 m/s and 2 m/s. The adaptability and shock absorption capacity of the proposed landing system is then evaluated and benchmarked against rigid legs. It reveals that the system is able to adapt to varied surface structures and reduce impact force by $540N$ at maximum. The bioinspired landing strategy presented in this paper opens a

promising avenue in Aerial Biorobotics, where a cross-disciplinary approach in vehicle control and navigation is combined with soft technologies, enabled with adaptive morphology.

1 Introduction

Unmanned aerial vehicles (UAVs) experience an ever-growing demand to perform reliably in real-world applications such as in post disaster rescue, pollution monitoring, ecology, infrastructure inspection and smart agriculture (Floreano and Wood, 2015). Small aerial robotic systems (in particular multirotor UAVs and related technologies) not only raise great interests in the robotics research community, but also lead to extensive development on the consumer market. One major focus of the current research in this field includes multifunctional robotic systems capable of flying, perching, gliding, climbing and manipulation (Low et al., 2015; Kalantari and Spenko, 2014) in unstructured outdoor environments. Seeking energy efficient locomotion, a jump-gliding miniature robot (Vidyasagar et al., 2015) is able to take-off from ground using high-power jumping mechanisms (Kovač et al., 2010), and uses gliding flight to effectively exploit the height gained after the boost for energy efficient mobility. To overcome limited endurance and restrictions on current battery capacity of small-scale aerial robots, the Stanford Climbing and Aerial Manoeuvring Platform (Pope et al., 2017) provides one promising solution which effectively combines directional attachment (Estrada et al., 2014) and climbing (Dickson and Clark, 2013) technologies. Other examples include adaptive morphology design principles for multimodal locomotion, such as the flying and walking robot, DALER, which is able to use its wings as legs to move on the ground, leading to effective and adaptive locomotion in different environments (Daler et al., 2013).

The efforts above explored a number of aerial robotic systems capable of perching and multimodal locomotion in unstructured environments. These studies demonstrated that dynamic transition between flight and landing is an essential phase of a complete flight mission for autonomously piloted multimodel UAVs. Looking closely at landing systems for small multirotor UAVs, there are various landing gear designs for small UAVs and Micro Aerial Vehicles (MAVs) for both scientific research and commercial production. However, most commercial designs have rigid frames (Fig.1(a)) aimed at vertical landing on flat surface of structured environments. In contrast to rigid frames widely used for commercial products, a number of interesting designs (Fig.1(b)-(f)) dedicated to simple linkage-based, movable landing gears have been explored recently. In these designs, either gravity powered passive actuation mechanisms or motor operated actuation mechanisms were employed. While these systems are simple and light-weight, their fixed design with a rigid

frame can lead to high impact forces on the UAV platform during landing, as well as blocked views of the onboard cameras and a largely restricted operating space for additional manipulators. Another challenge is that passive actuation mechanisms have difficulties to keep the UAVs in balance and remain upright with pure friction between grippers and structures.

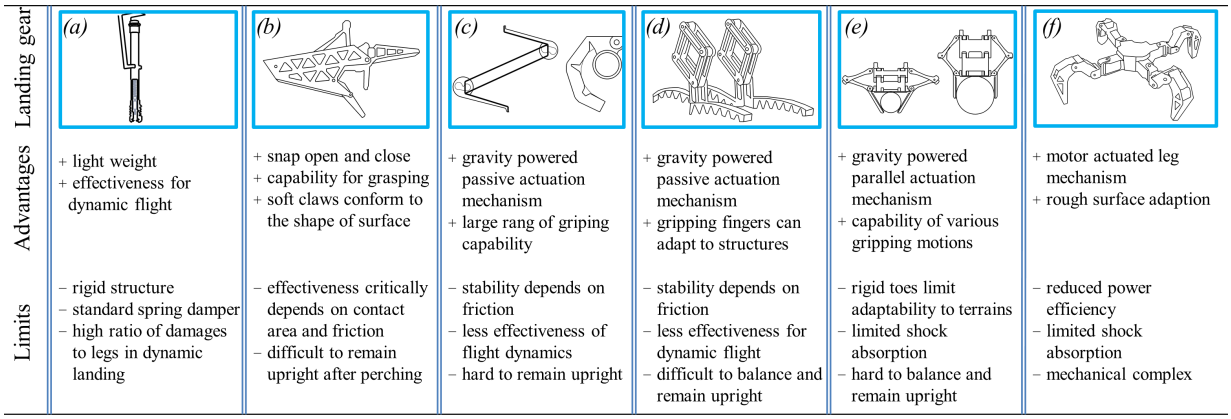

Figure 1: Designs of landing mechanisms for UAVs especially for multicopters: (a) the rigid landing gear with pneumatic shock absorber of DJI M100 (MATRICE 100 quadcopter for developers, 2015), (b) a snapping claw mechanism based design with soft claws (Culler et al., 2012), (c) a passive actuation mechanism with tendon driven claws (Doyle et al., 2013), (d) a four-bar linkage-based landing mechanism with compliant gripping digits (Tieu et al., 2016), (e) a Sarrus linage based landing mechanism (Burroughs et al., 2016), (f) a landing mechanism based on legged robots (Luo et al., 2016).

Though high impact energy arise from dynamic landing, it was rarely taken into account in most of the designs of small-scale aerial robotic systems for real-world applications. To facilitate dynamic landing of aerial robots in various terrain structures, weather conditions, landing modes and speeds, the landing mechanisms need to be adaptable to varied surface structures and functional for absorbing the impact energy. This is particularly important for dynamic landing manoeuvres at fast speed, where the impact energy can reach high values that can damage the vehicle frame, sensitive cameras and other electronics onboard. Further, the leg mechanisms have to be light-weight, given the limited payload capacity of these small aerial robots.

A recent cross-disciplinary study of adopting origami-folding technologies in engineering applications revealed that origami-inspired mechanisms based on foldable tessellations have great potential for energy absorption applications (Tolman et al., 2014). Examples include the thin-walled energy absorption devices (Song et al., 2012; Ma and You, 2014; Ma et al., 2016) for transportation vehicles. Further, engineering principles were applied to the performance evaluation of foldable origami artefacts in artistic disciplines, leading to novel solutions to various engineering problems in real world applications (Kuribayashi et al., 2006; Dollar et al., 2015; Zhang et al., 2015).

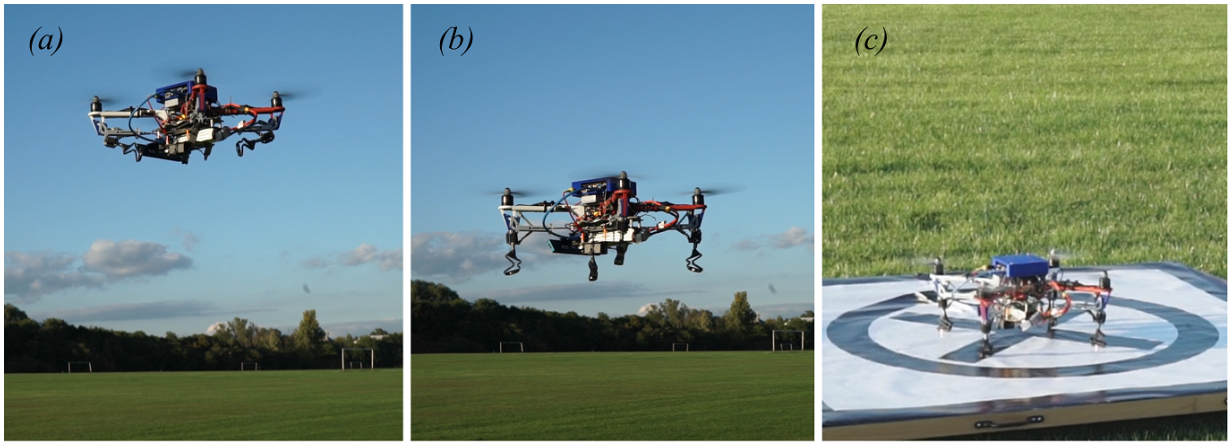

Figure 2: The autonomous quadrotor UAV, designed and built at the Aerial Robotics Lab with an 1-DOF retractable landing mechanism, performing an alighting manoeuvre: (a) the pre-landing stable flight with retracted landing gear, (b) approaching the landing site with deployed landing gear, (c) successful landing on the target.

In this work, we first review biological landing mechanisms and explore the landing methods, with a particular focus on the principles of legs and the sensory system commonly used by animal flyers, such as the honey bees, vampire bats and a steppe eagle. Taking the biological landing techniques of the animal flyers as a source of inspiration, we abstract key functions of different types of legs and sensory systems to inform the design of a landing mechanism for small aerial robots such as the quadrotor UAV in this work.

With the abstracted functions as guidance of practical design, this paper proposes a new adaptive landing mechanism for autonomous aerial robots in a way of combining both advanced flight control based on an onboard visual sensory system and resilience of 3D printable soft shock absorbers and landing pads.

The focus and contributions of this work are:

1. A aerial robot (Fig.2) capable of performing autonomous landing manoeuvres by adopting combined visual-inertial guidance and mechanical landing system, built upon the *inspire-abstract-implement* design paradigm.

2. A novel design for an adaptive landing mechanism that allows active morphing in accordance with flight phases and damped landing on varied structures and terrain.

3. The design and fabrication process of soft shock absorbers with shell mechanisms and soft landing pads with living hinges, that can both be 3D printed with various materials, such as thermoplastic composite materials.

In the following sections we first review the landing strategies of flying animals and abstract landing methods and techniques that can be adopted by autonomous aerial robots for performing safe landing manoeuvres. Taking inspiration from animal flyers, we present an overview of the system of the proposed autonomous aerial robotic system in Section 3, and the design and analysis, fabrication, and experimental characterization of 3D printable shell mechanisms and soft landing pads in Section 4. With a fully integrated prototype of the proposed robotic system, we then validate and benchmark the performances of the landing system in Section 5, and lay out conclusions in Section 6.

2 The Bio-inspired Strategy and Mechanism for Autonomous Landing

2.1 Brief Review on Biological Principles during Landing Manoeuvres

The study of natural systems revealed that evolutionary adaptation enables objects and processes in nature to be highly effective and robust (Kovač, 2016; Bhushan, 2009). Whilst the natural world evolves, its processes provides an extensive source of inspiration for creating comprehensive models of artificial systems that can mimic certain functions of their counterparts in nature (Manzanera and Smith, 2015). The bio-inspired design paradigm (Kovač, 2014) and perching principles (Roderick et al., 2017; Liu et al., 2016) provide cross-disciplinary approaches to developing new devices by mimicking the natural world in the way of adopting concepts and principles in nature in order to solve engineering challenges.

Powered and unpowered flight is a unique form of locomotion used by living species such as insects, birds and gliding mammals with variuos landing manoeuvres being adopted by each (Manzanera and Smith, 2015). Analysing and learning from the landing techniques of these animal flyers in nature can guide us to generate innovative ideas and concepts for the design of effective and robust landing systems of small aerial robots.

The overall landing strategy of animal flyers and gliders consists of comprehensive techniques, where behaviours are combined with sensing and actuation of wings, tail, legs and other body structures. In nature, dynamic landing combines aerodynamics, multi-modal sensing and learning. This paper focuses on reviewing and extracting the physical aspects of the landing process, with particular attention to how legs can be designed to damp impact during the dynamic transition phases between flight and landing.

Here we briefly review the functions of legs in selected examples of animal flyers, from insects, birds and

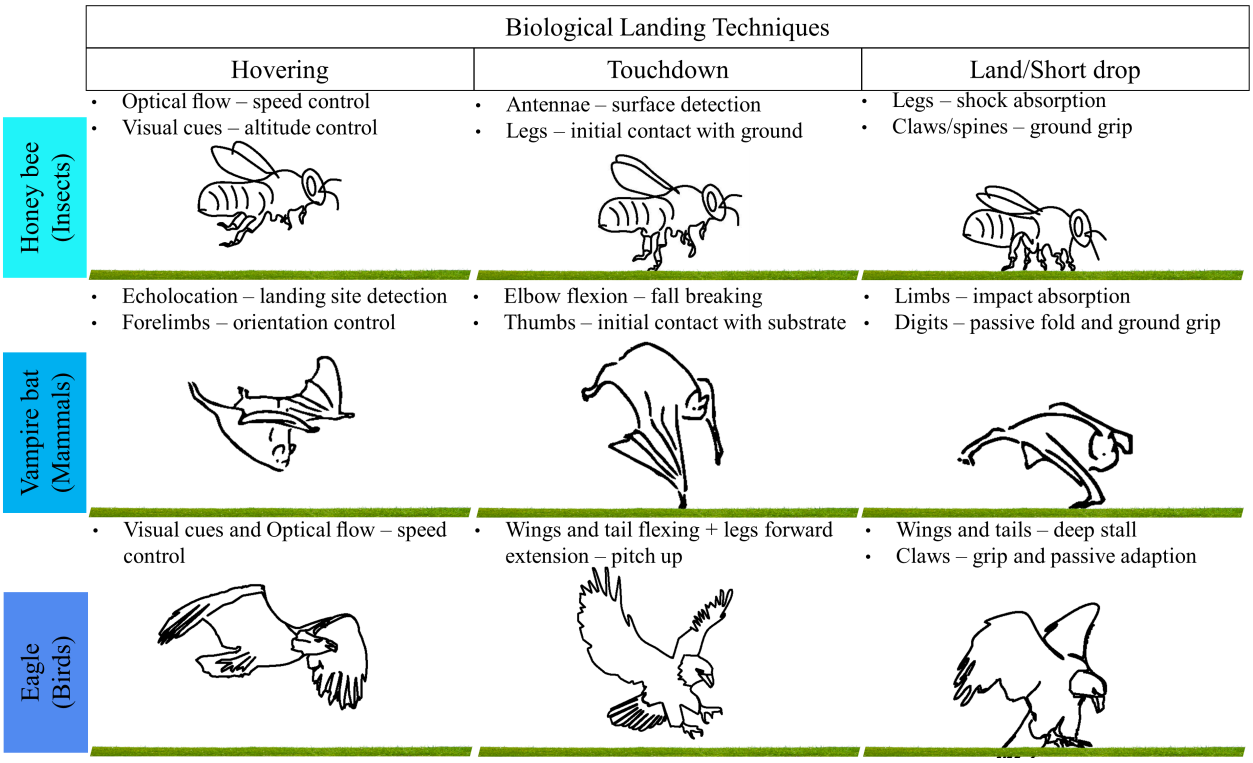

Figure 3: Computer restructured key frames of animal flyers (Manzanera and Smith, 2015) during alighting manoeuvres and abstracted landing methods, including leg mechanisms and sensor systems adopted by representative living species of insects, mammals and birds. The first row illustrates the sequence of leg movements during the transition from hover to land of the honey bee (Evangelista et al., 2010); the second row shows the elbow extension, thumb touchdown and dorsolateral bending during the short quadrupedal drop of Vampire bats (Altenbach, 1979); the last row shows the legs of an eagle extending forward, and the fully stretched configuration before the final short bipedal drop (Carruthers et al., 2007a; Carruthers et al., 2007b).

mammals, as illustrated in the ascending order of size in Fig.2. More detailed reviews of landing strategies in the animal kingdom can be found in literature (Kovač, 2016; Manzanera and Smith, 2015; Evangelista et al., 2010; Altenbach, 1979; Carruthers et al., 2007a; Carruthers et al., 2007b).

The honey bee (Apis mellifera) (Evangelista et al., 2010) uses optic flow and stereo-vision to approach the landing surface, and then enters into a quasi-hover state close to the surface (Fig.3(a)). Subsequently, it performs a stable hover while extending its legs to land with the hind and middle legs touching the surface. Although the impact speed is very small due to the hovering position prior to landing, the legs act as impact energy absorbers of the short drop by touching the ground (Manzanera and Smith, 2015).

The manoeuvres in the landing phase of the Vampire bat are different from the approach taken by bees, and can vary depending on the flight stage prior to alighting. A simplified three-stage procedure of a typical alighting manoeuvre on horizontal surface from hovering flight is shown in Fig.3(b). An interesting feature

in the landing of a Vampire bat is that its elbows have a pronounced extension, with the thumbs being aligned nearly in line with the long axis of the forearms prior to contact with the surface. While the thumbs touch the ground, they bend upward at the metacarpophalangeal joints to absorb the impact and adapt to the surface structure (Altenbach, 1979). This is followed by dorsolateral bending of the first metacarpal and the touching of the carpi to the surface. The pectoral limbs take in nearly all of the energy during dynamic landing, whilst the hind limbs act as stabilisers after impact with the surface. The mechanisms allowing Vampire bats to land at relatively high speed demonstrate a promising solution for the dynamic landing of small aerial robots.

Steppe eagles (Aquila nipalensis) take yet a different strategy. First the eagle stretches its legs in the forward direction in the second phase of landing manoeuvre as illustrated in Fig.3(c) while the fully extended wings act as aerodynamic breaks to aid deceleration. This strategy relies heavily on using wing morphing to adapt the landing velocity before impact, in combination with visual sensing (Carruthers et al., 2007a; Carruthers et al., 2007b).

By analysing above biological landing mechanisms, we can abstract the landing methods with a particular focus on principles of the legs and the sensory systems.

The following principles are identified to have promise for being implemented in the phases of landing manoeuvre of aerial robots.

1. Vision based sensory system that guides the approach behaviours and mechanical adaptability for a robust landing on a target position on the surface.
2. Two-level adaptivity of the damping structure, with the first level to locally adapt to surface architecture and second level to damp the high impact.
3. Mechanical adaptability of the soft landing pad to the surface, using mechanical reflex in the design of the system without the need for surface sensing and complex control.

2.2 The Strategy Inspired by Biological Landing Techniques

Here we present our general strategy to achieve dynamic landing in a representative landing scenario in the finals of the The Mohamed Bin Zayed International Robotics Challenge 2017 (MBZIRC2017)[1], which

[1]The Mohamed Bin Zayed International Robotics Challenge (MBZIRC) is an international robotics competition, which aims to provide an environment that harbours innovation and technical excellence, while encouraging spectacular performance with robotics technologies.

requires the Micro Aerial Vehicle (MAV) to land on a horizontal surface on top of a car moving at various speed. Inspired by the landing techniques of animal flyers, we have divided the mission of searching the moving platform and alighting the MAV on target into following steps:

1. Automatic take-off with a robust vision-based autopilot employing visual-inertial SLAM and Model-Predictive Control (MPC).
2. Search for the landing pattern on moving vehicle with the use of visual detection and tracking.
3. Approach the landing pattern on top of the moving vehicle with accurate tracking and motion prediction.
4. Landing the MAV with the use of a retractable landing system employing 3D printable shock absorbers and soft landing pads with magnets.

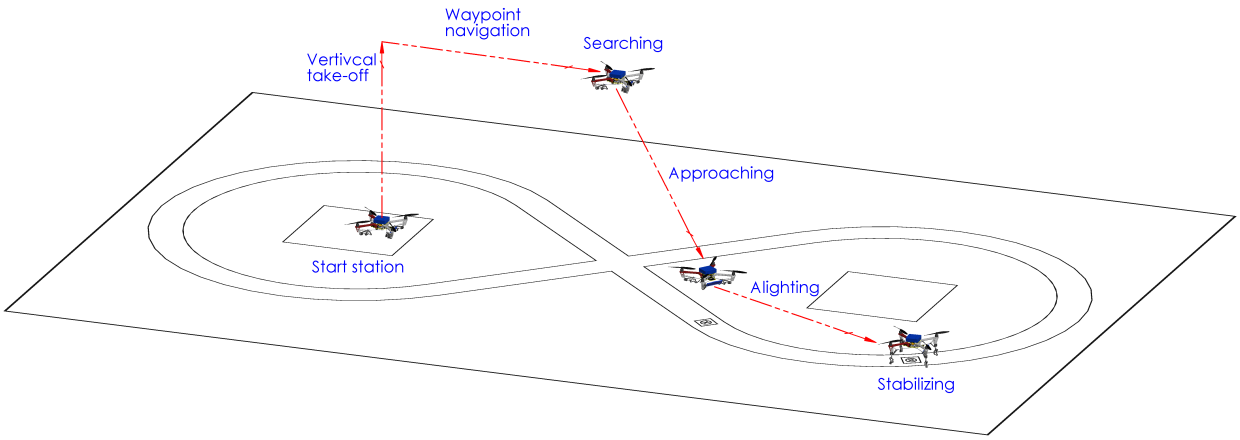

Figure 4: General strategy for alighting the MAV on the horizontal surface of a moving target (in the flight arena (1:1000) of MBZIRC competition). (a) Before taking off: the robot in stationary mode at the start location. (b) After vertical take-off: the robot reaches a certain height and starts searching the moving target with landing pattern on top. (c) The robot approaches the moving vehicle with automated motion prediction. (d) Landing mechanism deploys from the folded stage, allowing soft contact between the landing pads and the target. (e) The landing pads bend upwards and the shock absorber deforms for energy absorption, whilst the the magnets on the landing pads attach to the platform to stabilize the MAV while as the target is still moving.

With the principles learned from animal flyers, our general approach to the landing manoeuvres of the quadrotor MAV consists of three corresponding phases (as illustrated in Fig. 4), including (a) approaching, (b) alighting and (c) stabilizing. This operation process will enable transitions from high speed descending flight to a short drop by combining robust visual guidance and mechanical resilience of the proposed leg mechanism.

Table 1: The MBZIRC Requirements and Technical Data of the Customized Aerial Robot

Characteristics	MBZIRC requirements	Design specifications
Flight time	20 min	10 min
Range	>100 x 60 m	2 km
Max size of the UAV	1.2 x 1.2 x 0.5 m	0.85 x 0.85 x 0.2 m
Max speed of the UVA	30 km/h	70-80 km/h
Weight of the UAV	NA	2 kg

3 System Overview of the Autonomous MAV

The constrains for optimizing the design of an autonomous MAV include the total weight of subsystems, high performance onboard computer and visual sensors (which are essential for facilitate the MAV to complete the mission in outdoor environment), as well as the size of landing pattern placed on top of the roof of the moving vehicle. With consideration of these constraints, we have used DJI F450 as the quadrotor platform and a modular open-architecture for the electronic hardware, to allow quick reconfiguration of the layout to match the details of MBZIRC2017 mission requirements. A 3D model of the MAV developed in this work with a DJI F450 frame is illustrated in Fig. 5. Here, we took the DJI Flamewheel F450, since its frame arms are made of ultra strength material, providing crash-worthiness and the flexibility and abundant assemble space for further customization. The technical data of the MAV platform and customized specifications are listed in Table 1.

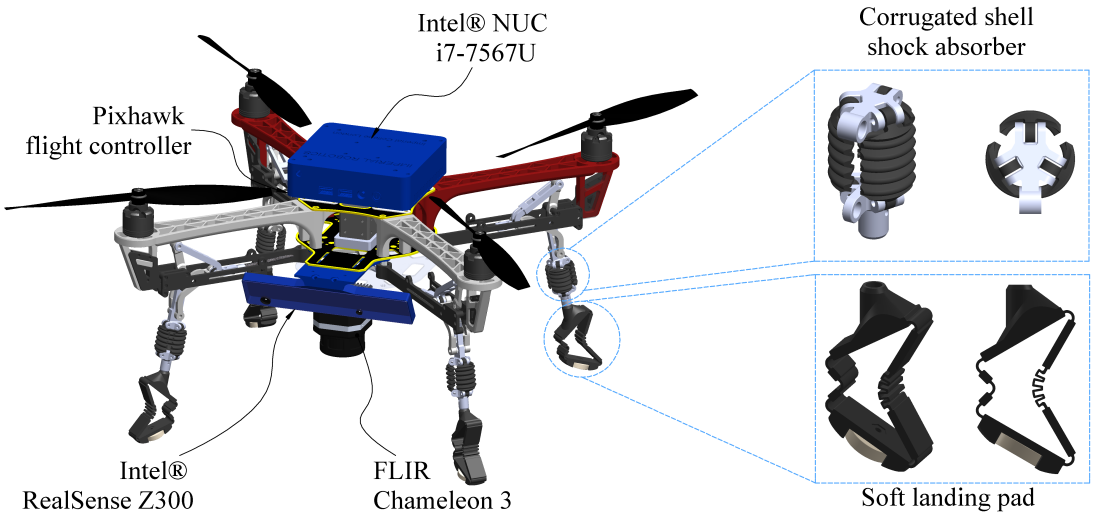

Figure 5: 3D model of the integrated quadrotor MAV with retractable landing gear, 3D printable shock absorbers, Intel NUCi7, Intel Realsense visual sensor and an additional downward looking camera.

3.1 Retractable Leg Mechanism with 3D Printable Soft Shock Absorbers

One of the critical challenge for MAVs is the limited payload capacity comparing to those large scale fixed wing drones and ground robots. It is always important to keep subsystems for small UAVs to be lightweight in order to maintain proper trade-off between flight duration and the added payload. In order to complete the MBZIRC2017 mission described in Section 2 within the shortest time, the quadrotor UAV requires aggressive and agile movement during the searching and approaching phases of the whole process in Fig. 4.

Taking all requirements above into account, we propose a new retractable leg mechanism which allows the MAV to fold its legs thus manoeuvre in a compact configuration in the same way of animal flyers while hovering and dynamic manoeuvring.

The penultimate stage-and one of the most important tasks of the challenge in MBZIRC2017-is to land the MAV on a moving target. This flight transition phase requires not only precise real time tracking, following and estimating of the moving target with the visual sensory system, but also mechanical robustness, allowing the MAV to alight on the horizontal surface and absorb shock energy associated with high speed landing as the MAV makes contact with the moving target.

Inspired by the biological landing techniques of animal flyers, particularly the use of extensible elements in their legs for shock absorption, this paper presents a new design of shock absorber with corrugated shell mechanisms (Fig.5) that can be fabricated with advanced multi-material additive manufacturing techniques (MacCurdy et al., 2016b; MacCurdy et al., 2016a). In this work, we selected Onyx, a printable composite material, made from combining tough nylon with micro-carbon fibre reinforcement (Markforged Materials, 2016) and the flexible Ultimaker thermoplastic polyurethane TPU95A (Ultimaker TPU 95A, 2017).

3.2 MAV Control and Navigation

We describe the software components for intelligence of the MAV in Fig.6. We follow a fairly classic decomposition of first estimating the state of the MAV, as well as the landing target followed by a controller to track a setpoint which in turn is determined by a higher-level guidance and state machine. Furthermore, we split the controller into a high-level Model-Predictive Controller, we developed ourselves and a low-level attitude and thrust controller employing an off-the-shelf Pixhawk module.

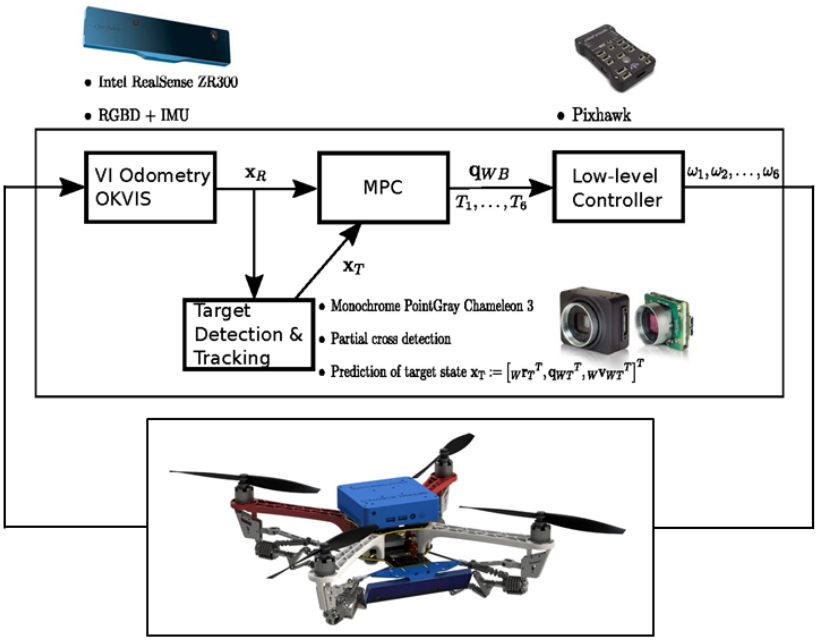

Figure 6: OKVIS (Leutenegger et al., 2014) is used in combination with the Intel RealSense ZR300 for the visual-inertial odometry estimation. The MAV state $\mathbf{x}_R$ is parsed to the target detection and tracking module. A monochrome FLIR Chameleon 3 is used for the detection. The target state $\mathbf{x}_T$ and the MAV state $\mathbf{x}_R$ are further used in the MPC to generate a reference quaternion $\mathbf{q}_{WB}$ and reference thrusts $T_1, \ldots, T_6$ for the low-level controller. A Pixhawk is used to convert the reference inputs to PWM signals $\omega_1, \ldots, \omega_6$.

3.2.1 State Estimation

As a basis for localisation of the MAV, we employ an extension of OKVIS: Open Keyframe-Based Visual-Inertial SLAM (Leutenegger et al., 2014). We have modified the formulation of the underlying estimator to use the RGB-D-inertial camera RealSense ZR300 instead of a stereo camera with integrated IMU. The underlying principle is inspired by ORB-SLAM 2 (Mur-Artal and Tardós, 2017), where we use depth measurements when available to create landmark observations in a virtual stereo camera.

In order to detect and track the moving target pattern as specified by the MBZIRC organisers, we use a downward-looking fisheye camera and assume the visual-inertial pose using OKVIS is known accurately enough. Initial detection follows a fairly straightforward, but highly optimised vision-processing pipeline to extract a quadrangle in the undistorted image, estimating the relative pose and verifying the appearance of the the landing pattern template. To track the target, even if it is only partly visible, we formulated an Extended Kalman Filter using a model of the dynamics in 3D space that assumes constant linear velocity and constant orientation in the prediction step. The update step then uses observations of the tracked keypoints of the pattern.

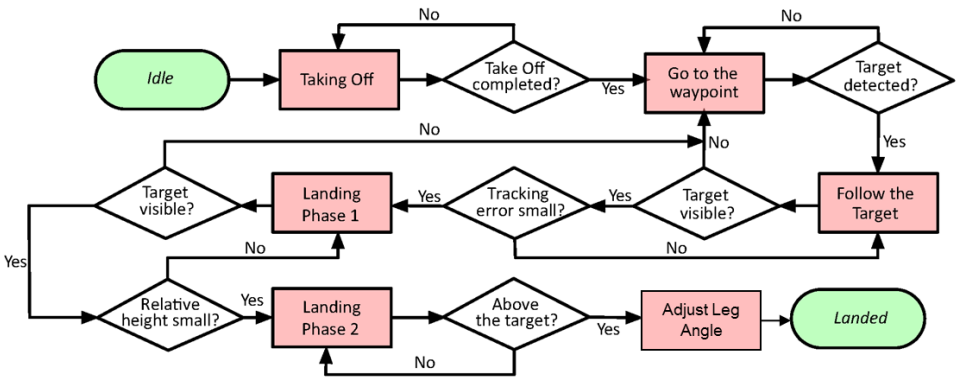

Figure 7: Flowchart indicating the transition between the various operating modes.

3.2.2 Controller

The MAV tracks the desired set-point using a cascaded control approach. Our high-level controller follows a linear Model-Predictive Control (MPC) approach to output tilt angles and thrust in order to track position and yaw angle. This is then followed by the low-level attitude and thrust controller, where we employ an off-the-shelf Pixhawk board. Finally, a high-level logic determines the current state set-point. First, commanding the drone to hover at the cross point of the figure-eight track (where we expect the vehicle with the landing pattern to pass through), secondly, following it to initiate descent, once the MAV has properly caught up. We describe this logic in more detail in Figure 7 depicting a flowchart with operating modes including the strategies in the case of target detection loss.

4 The Novel Retractable Landing System with 3D Printable Shell Mechanisms for Shock Absorption

The landing techniques that are employed by animal flyers as shown in Section 2 illustrate that body compliance of the leg mechanisms are salient features allowing them to perform dynamic landing. In particular, the following three main functions are important features for dynamic landing and are abstracted here for implementation in the aerial robots.

1. Absorb much of the energy arising from landing,
2. Grip to ground/structure with claws, spins and other techniques,
3. Fold-up in flight and extend/stretch during landing.

These functions need to be implemented on the aerial robot using light-weight and robust mechanical solutions. One type of interesting mechanical systems with both rigid and compliant elements are the foldable origami inspired mechanisms, in which the hinges are made from materials with multilayer laminates (Dai and Cannella, 2008) with inherent compliance. In contrast to rigid-bodied mechanisms, one attractive feature of origami-inspired mechanisms is the possibility to design their kinematics and compliance by taking the properties of materials into account (Greenberg et al., 2011). With the inherent flexibility of the compliant joints, the origami-inspired mechanisms have been widely utilized in robotic systems as compliant manipulators, limbs of walking robots and end-effectors of positioning devices (Li et al., 2017; Salerno et al., 2016).

In this section, we first present the designs of a new Sarrus shock absorber and a soft landing pad, which employ 3D printable compliant shells allowing large bending deformation thus absorbing impact energy. The performance of the individual shell mechanism, the Sarrus shock absorber and the landing pad are systematically investigated through FEA simulation, fabrication and experimental characterization. We then introduce the design of a 1-DOF actuation mechanism which allows the landing legs to fold into a compact configuration for agile manoeuvre and deploy for landing in a similar way as animal flyers.

4.1 Design and FEA Simulation of the Compliant Shell Mechanisms

To facilitate high speed dynamic landing on both static and moving targets, we present the Sarrus shock absorber with 3D printable shell mechanisms. The compliant shell mechanisms for large range bending are designed with consideration of the dimension constraints and the maximum take-off-weight of the MAV.

4.1.1 Morphing of curved corrugated shells

Corrugated sheets that are also curved along their corrugations (Norman et al., 2009; Seffen, 2012) can be transformed into a remarkable variety of shapes by simple bending of the surface. Figure 8 shows a design for a module with a corrugated shell that is initially curved along the corrugation axes. The perspective view of the corrugated shell is illustrated in Fig. 8(a), where various curvature is associated with the marked strip in Fig. 8(b). The coordinate systems including (X, Y, Z) in the equivalent mid-surface of the corrugated shells and the local coordinate frame (x,y,z) are given in Fig. 8(b). The geometry of the shell mechanism is defined by k_{XX}, the overall cylindrical curvature, k_g, the geodesic curvature, and k_{xx}, the local out-of-plane shell curvature of the specified strip. The performance of the shell mechanism are also determined by the thickness and the material properties.

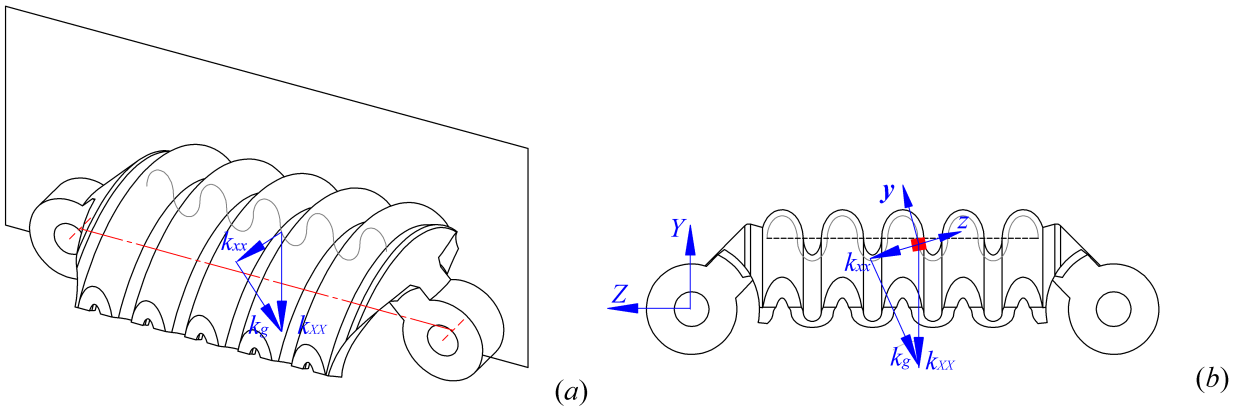

Figure 8: The curved corrugated shell mechanism. (a) 3D model of the shell mechanism, (b) curvature definition and coordinate systems

As the thickness and materials of the shells are varying in accordance with the fabrication process, we investigate the performance of the shell mechanism (Fig.8) using a finite-element-analysis (FEA) simulation approach first.

The nonlinear static Finite Element Analysis was conducted using ABAQUS package to simulate the compressed displacement and reactions of the corrugated shells. Since the sections at the two ends of the shell mechanism are significantly thicker than the shells and are freely rotating about two parallel axes, we assumed these sections do not affect the compliance of the test sample under pure compression in the Z-axis direction.

In the simulation, the Young's modulus of the Onyx material was set to be $1400MPa$ as reported by the manufacturer (Markforged Materials, 2016). A single corrugated shell mechanism was meshed using 60000 standard 3D stress quadratic tetrahedron elements. The corrugated shell mechanism was constrained in the hinges: only rotation around the X-axis was allowed on the side where the axis of the hinge is collinear with the X-axis, while the rotation around the X-axis and the displacement in the load direction were allowed on the other side. The boundary conditions were set to the reference points in the middle of the hinges with the reference points fixed to the hinges area using multi-point constraints. With current design parameters of the shell mechanism, a displacement of $10mm$ along the Z-axis was set to avoid any self contact in both simulation and experiment.

The rotation for the nodes that were allowed to rotate (hinge area) is shown in Fig. 9(b). It reveals that the angular displacement of the two hinges which are rotating in opposite directions is $0.8radians$. The performance shown that the shell can be inextensibly deformed to a howl-shaped curvature and the body

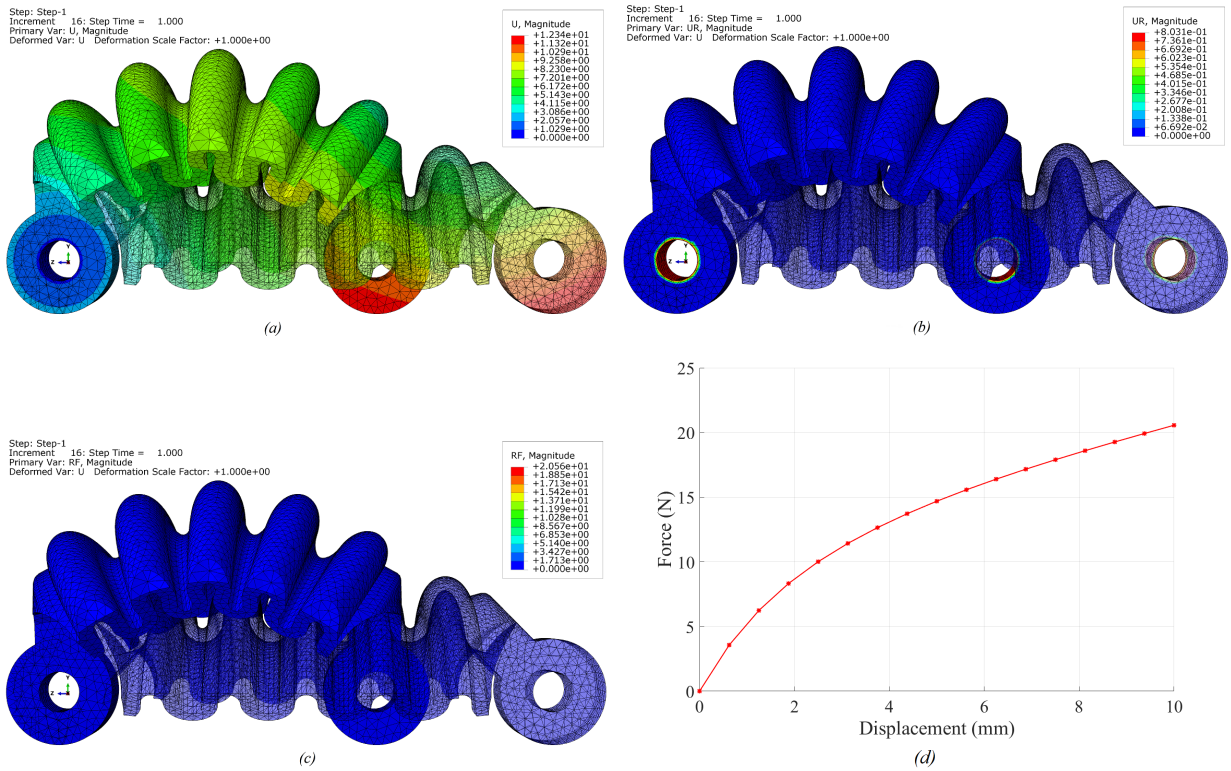

Figure 9: FEA analysis results of the shell mechanism. (a) displacement on the Z-axis (U3) direction, (b) rotation of the hinges about their axes, (c) reaction force on the Z-axis (RF3) direction, (d) reaction force-displacement curve

compliance which is important for dynamic landing.

The simulated results of reaction force and axial displacement of the deformed model are illustrated in Fig. 9(c) and the corresponding force-displacement curve is shown in Fig. 9(d).

4.1.2 The Sarrus shock-absorber with three shell mechanisms

In comparison with serial mechanisms, parallel mechanisms generally have higher stiffness and have been widely used in a wide variety of applications including large scale industry robots and nano-manipulators. A typical example of a parallel mechanism is the Sarrus linkage known as space crank that can transform circular arc motion of a hinge to a linear straight line motion. It can have several limbs consisting of two rigid links and three conventional hinges moving like elbows in parallel.

The simulation results of the shell mechanism (Fig. 9) show that the shells are able to transform bending deformation to a linear straight line motion under external compression. We propose a new design of compliant shock-absorber by replacing conventional rigid-bodied limbs of a three-sided Sarrus linkage with

the compliant shell mechanism. This leads to the Sarrus shock absorber (Fig. 10) with each compliant shell mechanism being connected to the upper and lower base by two hinges with parallel axes. By introducing the compliant shell mechanisms into the Sarrus linkage, the derived shock-absorber allows not only linear straight line motion like in conventional Sarrus linkages but also slight bending motion due to the compliant elements.

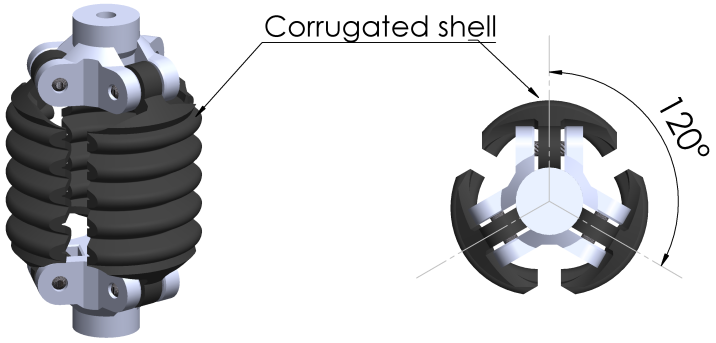

Figure 10: The compliant Sarrus linkage with curved corrugated shells for shock absorption: isometric (left) and top (right) views

4.2 The Soft Landing Pad with Compliant Hinges

Further to the Sarrus shock absorber which allows mainly linear straight line motion, we introduce a soft landing pad to absorb a small amount of landing impact energy and to bring in flexibility to allow bend and twist motion and thus adaptability to varied landing surface. The soft landing pad is a symmetric foldable planar 6R linkage, of which the design is based on the principles of thick panel origami-structures with hinges in single-curvature-shell shape and corrugated shell (Fig. 11). In the original shape of the design, the two largest thick panels form an acute angle of 60°.

With the thick panel origami inspired design, the inherent compliance of the soft landing pad is mainly determined by thickness as well as material properties of the compliant hinges. Under external loads, the compliant hinges are able to deform and thus change to folded configuration under compression and to stretched configuration under extension.

The inherent compliance of the soft landing pad is then simulated for identifying the thickness of the compliant hinges using various soft materials including Markforged Onyx and Ultimaker TPU95A filaments.

The coordinate frame was set up with the X-axis parallel to the symmetric plane of the linkage, the Y-axis perpendicular to the symmetric plane and pointing upwards and the Z-axis defined using the right-hand

rule. To simulate the performance of the shell mechanism under pure compression in the Y-axis direction, the nonlinear static Finite Element Analysis was conducted to simulate the compressed displacement and reactions. The Onyx filament is selected as the material and the Young's modulus was set to be $1400MPa$ (Markforged Materials, 2016).

In the simulation, the upper largest panel of the landing pad was constrained. The boundary conditions were set to reference points on the top face of the upper largest panel using reference geometry constraints. Under axial compression along Y-axis, the deformation of all compliant hinges allow the lower largest panel to rotate more than 30° and thus adapt to a large range of landing structures. The simulation results of the large range bending and reaction force of the deformed model are illustrated in Fig. 11.

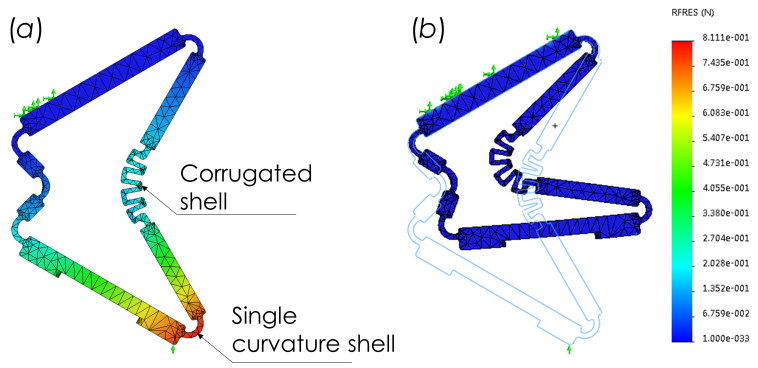

Figure 11: The foldable landing pad with corrugated shell elements capable of large range of bending. (a) original meshed model in symmetric shape, (b) FEA simulated resultant reaction force using Markforged Onyx material.

To achieve the key function of gripping to structure, we added a magnet at bottom of each landing pad to allow the robot to attach to the platform stably. In other words, the magnets allow the MAV to grip to various magnetic friendly structures in different shapes particular moving targets without bouncing off.

4.3 Fabrication of the Corrugated Shell and Landing Pad with Printable Composite Materials

Traditionally, corrugated shells are made by vacuum-forming a sheet of thin layered materials such as High-Impact Polystyrene (HIPS) (Norman et al., 2009). However, the process is rather complex and takes longer fabrication time compared to 3D printing techniques.

Multi-material additive manufacturing techniques offer a compelling alternative fabrication approach, allowing materials with diverse mechanical properties to be placed at arbitrary locations within a structure.

The Markforged Two, one of the 3D printers used in this work, is capable of depositing three different materials including continuous carbon fibre and fibreglass for fabricating versatile parts with fibre reinforced thermoplastics. The printer can achieve a finished-part resolution at 100 micrometers. Another 3D printer for printing the soft landing pads using TPU95A is the latest Ultimaker3, which support a large range of thermoplastic materials and polyvinyl alcohol (PVA), which is a water-soluble support material for multi-extrusion 3D printing.

In order to explore the performance of the 3D printed shell mechanisms presented above, various part settings and material settings have been used for printing samples for experimental tests and for comparison with the simulated results. The part settings include the type of supports, supports angle and layer height which is also known as resolution of printing. The material settings include the fill pattern, fill density, roof and floor layers and number of wall layers. By changing these settings, the printing time and the quality of the parts are varying. The final setting for these parameters in this work was selected based on comparison between results from simulation and tests of samples.

The design parameters, in particular the thickness of the thin wall structure, have to be tuned to allow solid fill of materials in both the corrugated shell and the single curvature shell. It needs to be mentioned here that a 100% fill density does not assure that the space between wall layers is fully filled. With the same setting of 100% fill density, not all the corrugated shells with various thickness from 0.7mm to 1.3mm are solid in reality as shown in the internal view of the shell mechanisms during printing (Fig. 12).

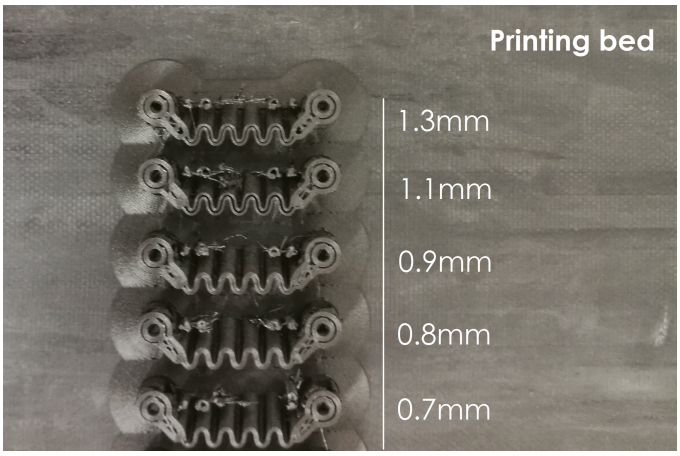

Figure 12: Internal view of practical fill density of materials in between wall layers with various thickness in design

The experimental tests of samples revealed that the layer height in the part settings play a significant role in affecting the performance of parts printed with pure plastic materials. Further, as Onyx and tough nylon

are thermoplastic materials, the environment conditions also affect the softness of 3D printed parts.

For statics characterization, the corrugated shell mechanisms were fabricated with $0.2mm$ layer height and triangular fill pattern at 100% density. This allows us to have practically fully filled compliant elements. For the landing pads printed with TPU95A, the print setting was customized with layer height at $0.06mm$ and 100% infill density to obtain the extra fine profile.

4.4 Statics Characterization of the Shock Absorber and Landing Pad

Having had samples 3D printing with the Markforged Onyx and Ultimaker TPU95A materials, we tested the properties and performance of the corrugated shell mechanism, the Sarrus shock absorber and the landing pad using a dynamic mechanical thermal analyser (DMTA)[2] and Instron test machines.

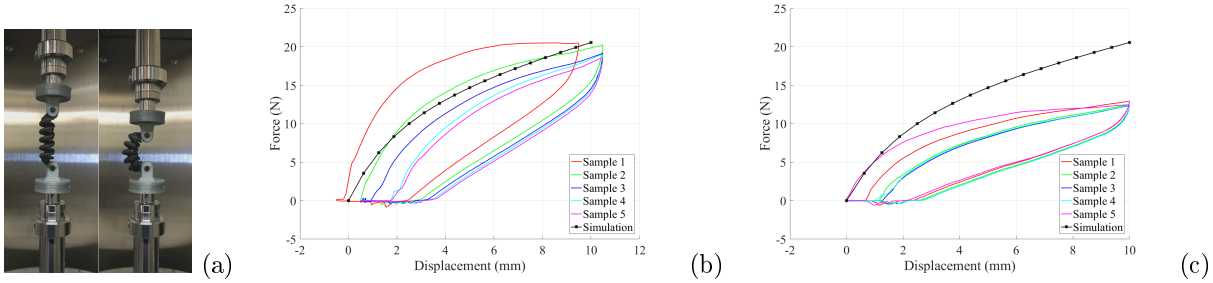

Figure 13: Experimental characterization of the corrugated shell mechanism. (a) original and compressed stages on DMTA, (b) reaction force of newly printed samples, (c) reaction force of samples under compression tests ($24hrs$ after completion of 3D printing)

The original and deformed configurations of the corrugated shell mechanism with final setting parameters are illustrated in Fig. 13(a). It reveals that the corrugated shell mechanism is capable of large range displacement under compression and returning to the original configuration after releasing of the load.

As shown in Fig.13(b), the tested reaction forces of newly printed samples of the corrugated shell match well with the simulated force-displacement curve. However, the performance can change over time due to properties of the materials employed. For instance, the reaction forces of samples exposed to normal lab environment for over $24hrs$ decreased significantly as the thermoplastic composites can absorb air moisture and becomes softer (Fig.13(c)).

The tested reaction forces in Fig. 14 of the Sarrus shock absorber also decreased due to moisture absorption after exposure to the normal lab environment for over $24hrs$. More tests would be used to study the long term

[2]The RSA-G2, which is the most advanced platform for mechanical analysis of solids, insures the purest mechanical data through independent control of deformation and measurement of stress.

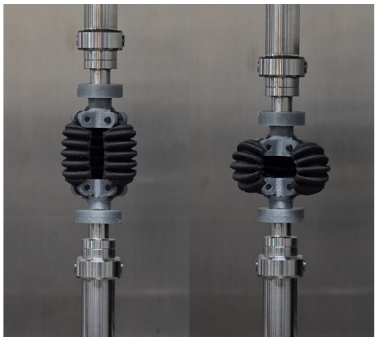

(a)

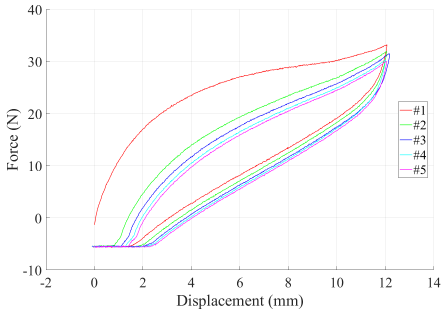

(b)

Figure 14: Experimental characterization of the Sarrus shock absorber. (a) original and compressed stages on DMTA, (b) reaction force of samples printed after $24hrs$

stability of the chosen materials and conclude on the effect of environmental factors such as rain, humidity, sun light etc.

In order to test the bending motion of the soft landing pad, a simple test rig was prepared and assembled to the landing pad before the experimental tests. During compression, the top panel is fixed to the upper fixture of DMTA test machine while the two roller wheels mounted on the lower panel rotate freely on the lower fixture of the machine. We assume the lateral force is negligible compared to the vertical axial compression. The deformations and resultant reaction forces of the soft landing pads printed with both Onyx and TPU materials are shown in Fig. 15.

4.5 The 1-DOF Actuation Mechanism for the Retractable Landing System

As listed above, one of the key function of the landing mechanism is to allow the legs to fold-up in dynamic flight manoeuvres and deploy during landing to adapt to varied surface structures where the MAV needs to land. To achieve these goals, we designed a new mechanism by integrating two planar linkages moving in two orthogonal planes, as illustrated in Fig.16.

As illustrated in Fig.16, the slider-crank mechanism consists of three revolute joints O, A and B and one prismatic joint with axis aligning with OB. The second planar linkage is a symmetric 5R linkage consists of joints C, D, E, E' and D' and all joint axes are perpendicular to the plane defined by the slider-crank mechanism. In other words, the axes of joints B and C of the part coupling these two linkages are orthogonal. With these physical and geometric constraints by two orthogonal planar linkages, the axis of joints B is restricted in the plane defined by the 5R linkage while the axis of joint C is restricted in the plane of the slider-crank mechanism. Hence, the assembly in Fig.16 is a 1-DOF spatial mechanism.

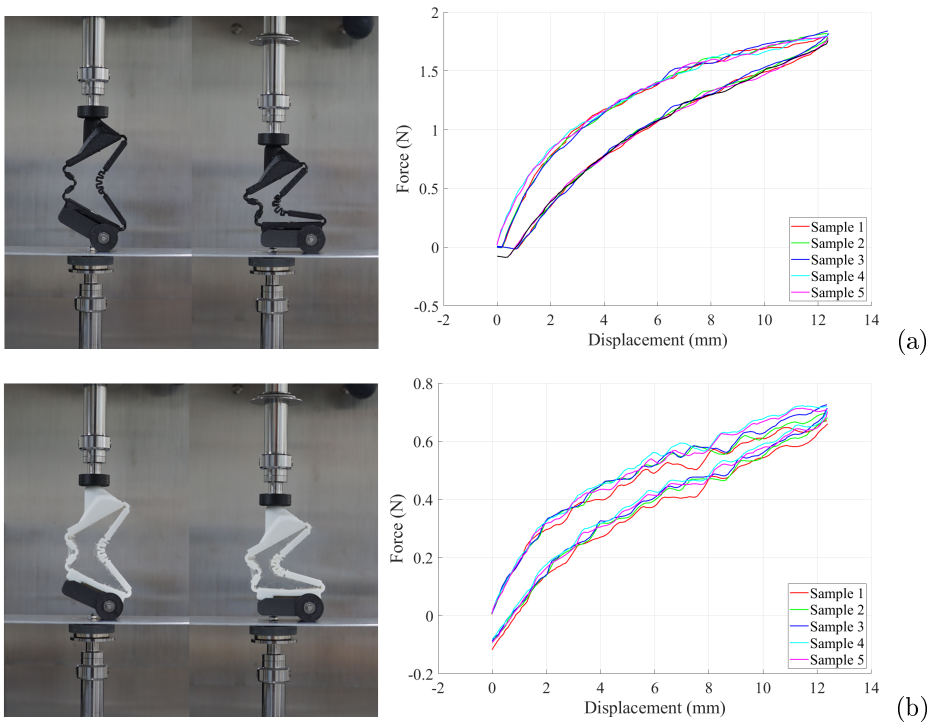

Figure 15: Experimental characterization of soft landing pads. (a) The deformation and reaction force of a landing pad printed with Markforged Onyx (b) The deformation and reaction force of a landing pad printed with Ultimaker TPU 95A. The soft landing pad using TPU 95A is more flexible than that using Markforged Onyx.

While the crank OA is rotating about axis of joint O with an angular input α, the link $D'E'$ of the 5R linkage moves accordingly with an angular displacement β measured between EE' and $D'E'$. When the crank OA input $\alpha = 0°$, the mechanism moves to the fully deployed configuration in Fig. 16(a) where the output angle β reaches the maximum value, 140°, of this design. This is a configuration of the leg mechanism where the crank slider mechanism is in its singular configuration and effectively locks the legs. The 5R linkage can be folded into a compact configuration in Fig. 16(c) with links DE and $D'E'$ parallel to OB. In this configuration, the angular input $\alpha = 86.73°$ and the output β reaches the minimum value, 0°. In between the fully deployed and compact configurations, the leg mechanism can adjust its configuration to adapt to various structures for landing. For instance, the configuration in Fig. 16(b) with output $\beta = 90°$ is suitable for landing the MAV on flat surfaces.

The leg mechanism in Fig. 16 is mounted underneath the airframe with the axis of joint O passing the mass centre of the MAV and parallel to the rotor axes. The base link EE' is fixed to the frame arm as illustrated in Fig. 5. The link $D'E'$ is connected to the Sarrus shock absorber for dissipating the main impact energy during dynamic landing.

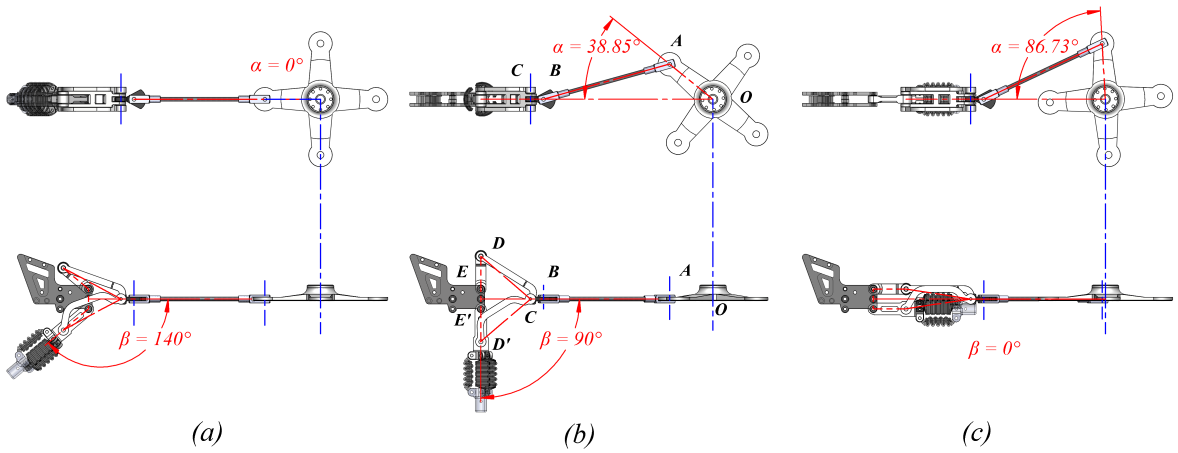

Figure 16: The 1-DOF retractable landing mechanism with two coplanar linkages moving in two orthogonal planes. (a) fully deployed configuration, $\alpha = 140°$, (b) configuration for vertical landing, $\beta = 90°$, (c) fold-up configuration, $\beta = 0°$.

The number of legs is determined by the number of frame arms and the MAV in this work has four legs. These legs are symmetrically distributed in the same pattern of the frame arms and operated by a single actuator driving the crank around axis of joint O. During the landing phases, the four retractable legs are configured to adapt to the geometry of surface structure for landing. While the MAV is in flight phases, the leg mechanisms are retracted to fully folded compact configuration.

5 Characterization and Benchmarking of the Morphable Leg System for Dynamic Landing on Various Environments

Following the 3D printing of the soft shock absorbers and landing pads, a complete prototype of the leg mechanism has been assembled and integrate with the MAV frame. Here we present test results of the fully integrated autonomous MAV in both indoor and outdoor environments.

The impact accelerations experienced by the quadrotor UAV have been recorded using ADXL377 accelerometer breakout board, which is rigidly attached to the frame of the quadrotor. The acceleration data stream has 3 axes: $[X, Y, Z]$ and they were recorded at a rate of $250Hz$. The accelerometer implements 10-bit analog output with $\pm$200g as an output range. This gives us a resolution approximately at $3.83m/s^2$ of the recorded acceleration. In the indoor environment, we implemented the landing tests in a Vicon motion capture system which is used as a source for position and landing velocity data, at $100Hz$, for the MAV control system. Following the indooir characterization, we then implemented the control and navigation

system in Section 3 in the field tests.

5.1 Vertical Landing on Static Targets with Soft Shock Absorbers and Landing Pads

In a similar way of animal flyers' short drop in the final stage of landing, the MAV cuts out the thrust and implements a free drop towards the surface structure to complete the last stage of a vertical landing once received the landing command. Before the short drop has been initiated, the quadrotor is hovering directly above the target position.

For the purpose of demonstrating the reconfigurability of the 1-DOF leg actuation mechanism and the adaptability to varied surface structure, landing tests have been implemented on three different structures including a horizontal flat plate, a convex surface structure and a concave surface structure.

Vertical landing tests were first implemented with horizontal flat surface structure, which was designed according to the specifications given by the challenge of MBZIRC2017.

As shown in the experimental results in Fig. 17, both X and Y components of the acceleration remained close to zero as the landing is completed with a vertical short drop. On the other hand, we observed two peaks, negative and positive, acceleration in Z-axis direction. Instead of having spontaneous and sudden impacts, the soft shock absorbers dissipate the impact energy by spreading the impact shock over time. The durations of these positive peaks can be seen to last about 50ms rather than one spike which lasts a mere millisecond for hard impact/crash (Briod et al., 2014).

Following the landing tests on flat surface structure, the landing system was further tested on both convex and concave surface structures respectively.

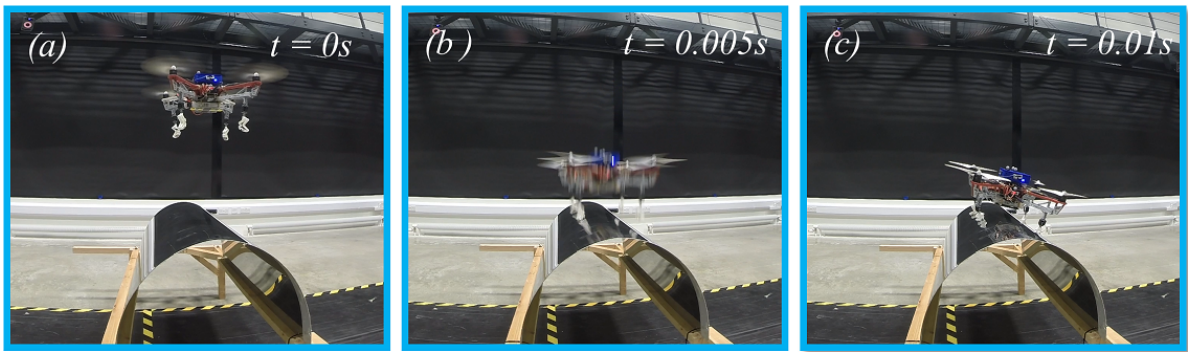

Figure 18: Indoor landing on convex surface structure with landing pad printed using TPU material: (a) hovering above the target position and start drop, (b) touchdown at $t = 0.005s$, (c) stabilized at $t = 0.01s$.

As illustrated in Fig. 18, a metal sheet of $1mm$ thickness was deformed to a convex surface structure of which the top section is a half cylinder with $R_1 = 254mm$. With this convex surface structure, the leg mechanism is open at $82.5°$ to adapt to the geometry. For these landing tests, we adopted same landing strategy and the quadrotor first hovers on the top of the target position and then completes the landing with a short drop. A total of 15 tests were implemented with average vertical touchdown speeds at $1.136m/s$, $1.618m/s$ and $1.994m/s$. The impact acceleration of these tests are reported in Fig.19. It reveals that both X and Y components of the acceleration increases as the robot tilts laterally to adapt to the surface structure, but they remained relatively small comparing to the component at Z direction.

For the tests on concave structure, a metal sheet was deformed to a concave surface structure in Fig. 20 with $R_2 = 654\ mm$. With this convex surface structure, the leg mechanism is open at $110°$ to adapt to the geometry. A total of 15 vertical landing tests were implemented with average vertical touchdown speeds at $1.034m/s$, $1.574m/s$ and $1.808m/s$ respectively. The impact acceleration of these tests are reported in Fig.21.

It revels that in the landing tests on convex and concave surface structures, both X and Y components of the acceleration also increases but remained relatively small comparing to the component at Z direction.

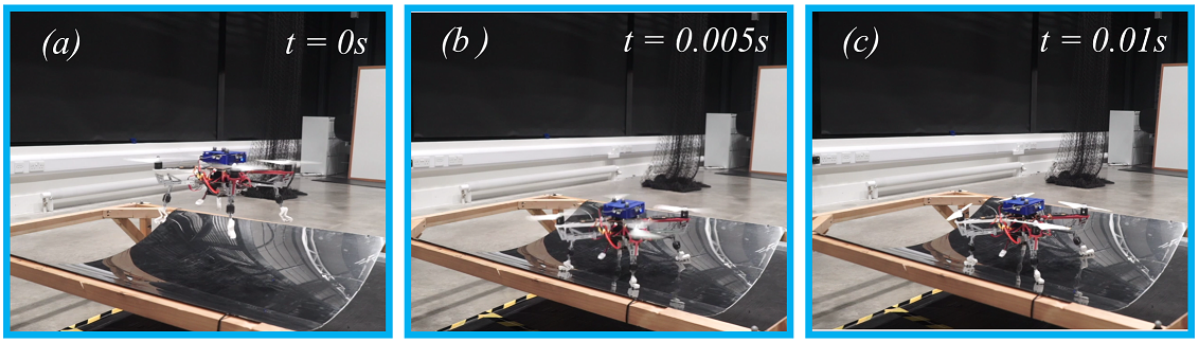

Figure 20: Indoor landing on concave surface structure with landing pad printed using TPU95A material: (a)hovering above the target position and start short drop, (b)touchdown at $t = 0.005s$, (c)stabilized at $t = 0.01s$.

5.2 Vertical Landing on Static Horizontal Flat Surface with Rigid Legs

Apart from the landing tests above, we further implemented same landing tests on horizontal flat surface with rigid legs. This allows us to characterize the design significance of the proposed soft shock absorbers by comparing the peak accelerations in the landing direction during a series of landings at different speed.

For the landing tests with rigid legs with average vertical touchdown speeds at $1.036m/s$, $1.546m/s$ and $2.076m/s$, we implemented 15 times landing tests of which 5 times for each landing velocity. The peak acceleration of each test is reported in Fig.22.

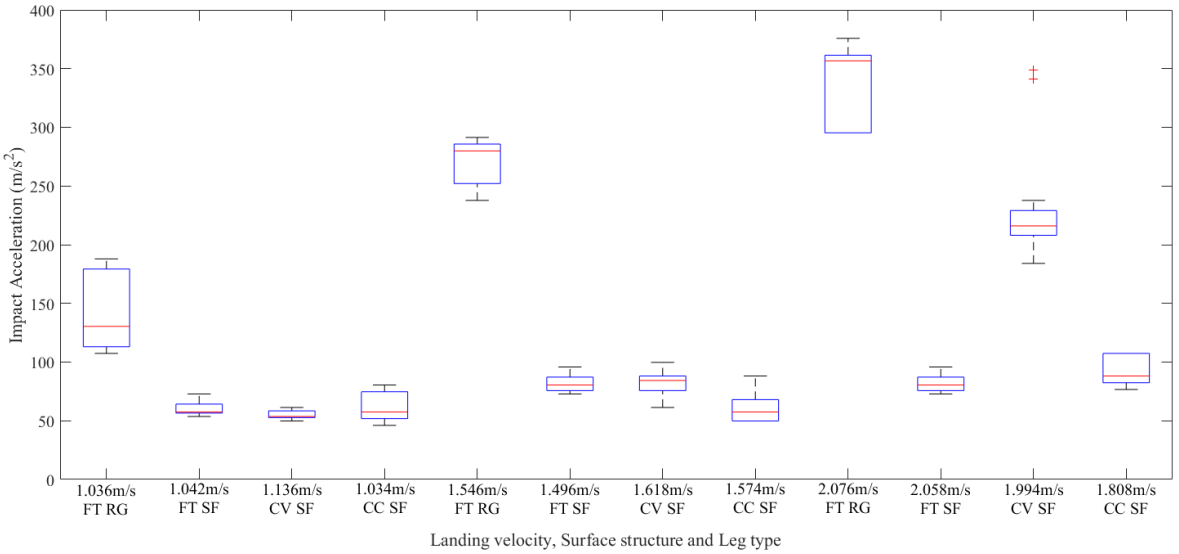

Figure 23: Comparison of the peak impact accelerations of landing tests on varied surface structures with different landing speeds: the peak acceleration is reduced in average by $65m/s^2$, $200m/s^2$ and $270m/s^2$ with reference landing speeds at $1m/s$, $1.5m/s$ and $2.0m/s$. (FT: Flat surface, CV: Convext surface, CC: Concave surface, RG: Rigid leges, SF: Soft legs)

Because the vertical impact acceleration is markedly larger compared to the anterior-posterior or medial-lateral components, the peak value of vertical components has been used for characterizing the capacity of absorbing impact energy.

The peak impact accelerations of all landing tests with soft shock absorbers are compared against that of rigid legs at average touchdown speeds referenced at $1m/s$, $1.5m/s$ and $2.0m/s$. The statistic box plot in Fig.23 explicitly illustrate that the vertical peak impact acceleration are significantly reduced in all tests with the soft shock absorbers and landing pads. Only those peak accelerations of landing tests on convex structure with average speed at $1.994m/s$ are higher than the other cases. The exceptional individual tests results with high value could be cases where the absorber were broken due to bending motions that exceeded the design ranges.

The comparison of results using soft legs and rigid legs reveals that the soft leg mechanism proposed in this

paper is capable of reducing the peak acceleration by $270m/s^2$, therefore dissipating $540N$ impact force at maximum.

From principle of momentum conservation, a quadrotor colliding with a static metal plate is expected to bounce up. However, this is not the case here because of the magnets mounted on the flat panel of the landing pad which touches the surface structure at first. Only small upward acceleration can be seen throughout all tests as the magnets is used to holding the MAV on the target position, which is particularly important while the target is moving.

5.3 Field Tests of Dynamic Landing on Grassy Field and a Moving Target

Experimental results in this section were obtained in outdoor field tests where the MAV landed on grassy field as well as a moving target that suits MBZIRC17 requirements. In the scenarios of vertical landing the MAV on dry grass ground and where the magnets are not necessary, the soft landing pad with magnets were removed and only the Sarrus shock absorbers were used to absorb the impact energy during landing (Fig. 24).

Figure 24: Outdoor landing on grassy field with Sarrus shock absorber: (a) hovering above the target position and start drop, (b) touchdown at $t = 0.005s$, (c) stabilized at $t = 0.01s$. The MAV landing at a speed higher than $1m/s$ always bounces off the ground after first touchdown. Gripping techniques are essential for stabilizing the MAV.

The tests results for vertical landing on grassy ground with average vertical landing speeds at $1.092m/s$, $1.438m/s$ and $2.102m/s$ are illustrated in Fig. 25. Comparing to the results of landing tests, in which magnets are used to allow the MAV to grip to the structure, in subsection 5.2, the landing tests on grassy field show larger lateral impact accelerations. This means that accelerations in the direction of X- and

Y-axis may not be negligible in certain landing scenarios. This can induce bounce off from landing surface and thus drop from the landing target moving at a high speed. Thus, gripping techniques are essential to allow the MAV to firmly grip to the target position.

In order to successfully land on a moving target, the MAV has to actively track the target while adjusting its attitude to achieve certain landing velocity. The outdoor flight tests were carried out following the mission strategy introduced in Section 2. The decomposed trajectories in X-, Y- and Z-axis directions in the global coordinate frame of one of the implemented flight tests are plot in Fig. 26(b). The autonomous tracking, approaching and landing phases on the moving target in the experiment is illustrated in Fig. 26(c), in which the frames are took with equal intervals in between. The varied poses of the quadrotor demonstrate the manoeuvres in response to the speed of the moving target on the ground. As a result, the MAV may land at non-vertical angle and produce some vibrations in acceleration data. However, similar trend as the indoor experiment can be observed from the data obtained in experimental tests.

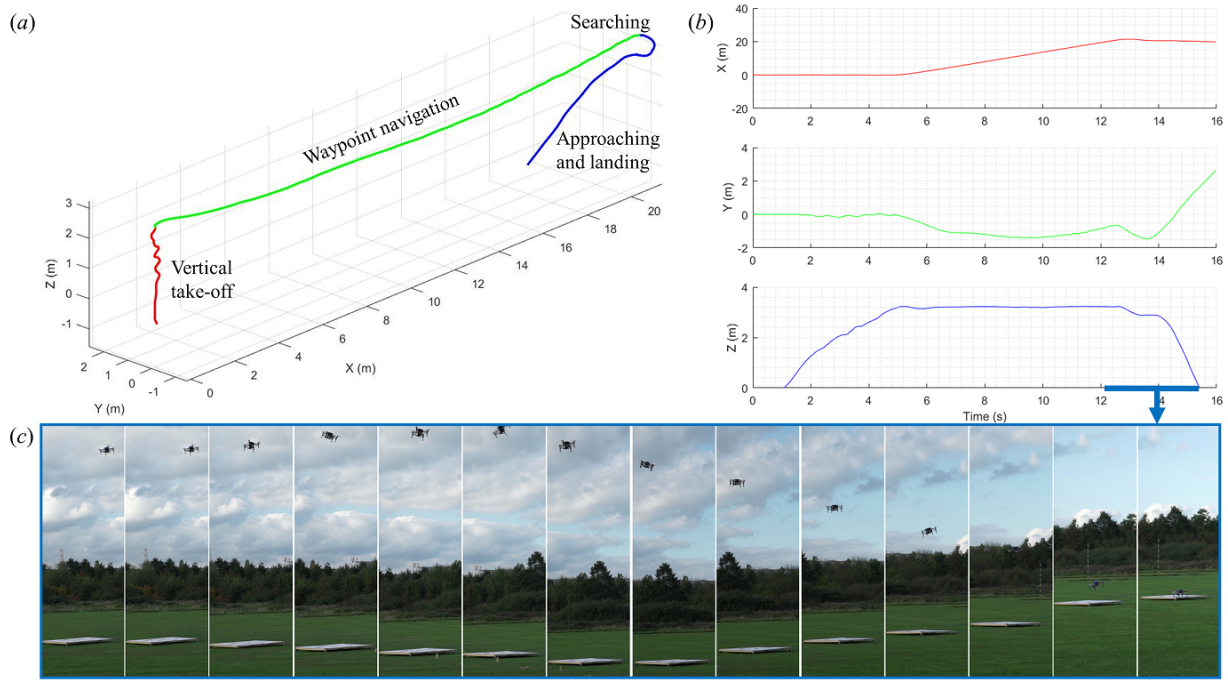

Figure 26: Outdoor test following the mission for landing on the moving target. (a) three dimensional trajectory of the planned mission, (b) decomposed trajectories of the approaching and landing phases, (c) flight manoeuvre sequence during the transition phase of landing on moving target.

In term of peak vertical impact acceleration, all 1 m/s velocity setpoint impact tests, both indoor and outdoor, yield approximately 50 m/s^2 or below for the peak impact shocks. In 1.5 m/s impact scenarios,

peak vertical impact shocks are about 80 m/s^2 and 100 m/s^2 for indoor and outdoor tests respectively. At highest impact velocity scenario, we observed values within 100 m/s^2 for indoor tests and within 150 m/s^2 for outdoor tests. This range of impact shocks is arguably within safe region for quadrotor UAV (Briod et al., 2014). The MAV does not show any sign of damages and deterioration of performance.

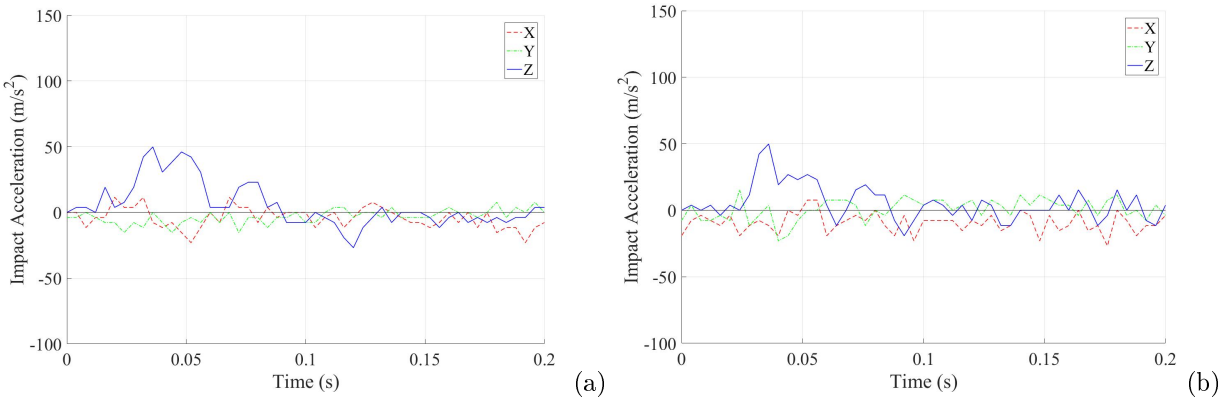

Figure 27: Outdoor tests on the moving target: Impact acceleration for 1 m/s velocity setpoint upon impact

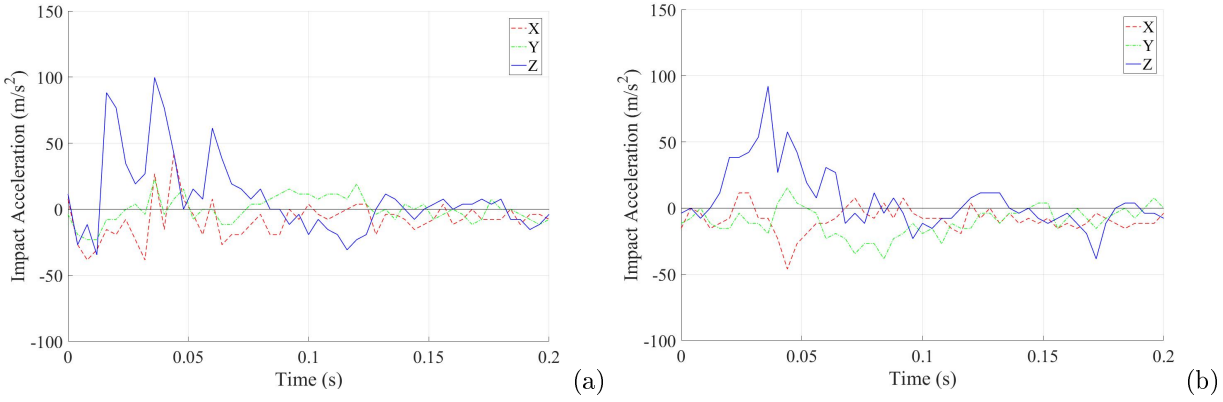

Figure 28: Outdoor tests on the moving target: Impact acceleration for 1.5 m/s velocity setpoint upon impact

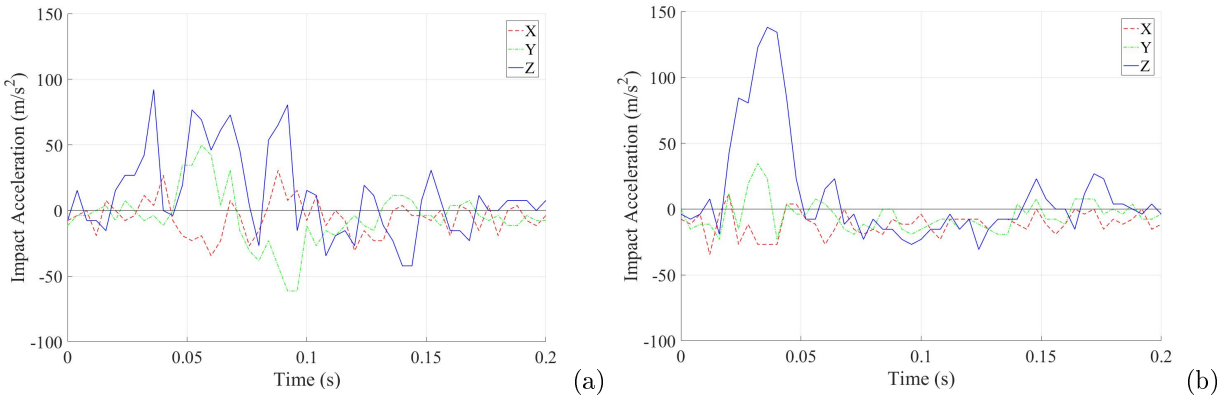

Figure 29: Outdoor tests on the moving target: Impact acceleration for 2 m/s velocity setpoint upon impact

With the impact acceleration obtained from the accelerometer during the outdoor landing tests, the impact force during the touchdown moment of landing can be then calculated given the mass of the robot is known. The impact forces of selected outdoor test trails where the robot did not bounce off with reference landing speed at $1m/s$, $1.5m/s$ and $2m/s$ are reported in Fig. 30, where maximum impact forces corresponding to each landing speed of the outdoor tests are $95N$ at $1m/s$, $197N$ at $1.5m/s$, and $295N$ at $2m/s$.

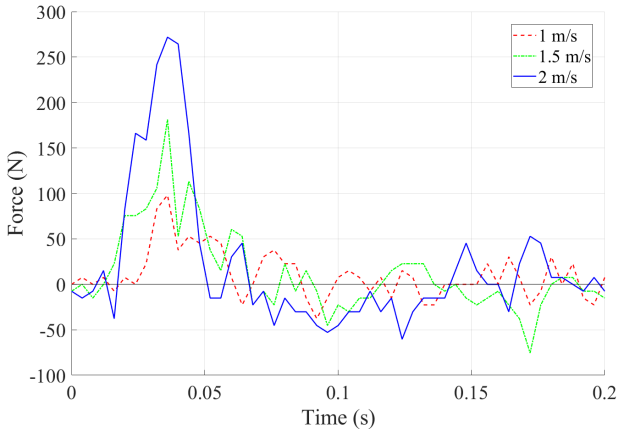

Figure 30: The evolution over the time of the contact force occurring during dynamic landing on moving target

6 Conclusions

The work in this paper explores bioinspired solutions in landing gear morphologies of small aerial robots to achieve dynamic landing on varied surface structures as well as moving targets. Taking inspiration of animal

flyers in nature, a landing strategy based on robust visual-inertial guidance and physical leg mechanism adaptability is adopted to safely land the aerial robot at a target position in real world applications. Built on the inspire-abstract-implement bioinspired design paradigm, a retractable leg system with a 1-DOF actuation mechanism was designed and realized for leg morphing in various flight modes of aerial robots mimicking the function of leg-extension in animal flyers. A morphable shell mechanism was designed as a compliant module of a new shock absorber based on the Sarrus linkage and shell structure based living hinges were employed in the design of a foldable landing pad. Both the morphing shell mechanism and the landing pad were then fabricated with advanced multi-material additive manufacturing process and flexible thermoplastic filaments. This leads to inherent softness of the shock absorber and landing pad which provide two-level adaptivity of the landing system. The first level adapts locally to surface architectures and the second level damps the high impact energy in the final stage of dynamic landing. The design of the origami-inspired corrugated shell mechanism and the soft landing pad were analysed using Finite Element Analysis (FEA) simulations and were evaluated with dynamic mechanical testing of 3D printed samples. The conceptual design of using 3D printable modules for dissipating impact energy during landing manoeuvres of small aerial robots were verified with vertical landing tests on three types of static surface structures, including horizontal flat surface, convex and concave surface structures, and outdoor flight tests on grassy field and a moving target. The peak accelerations during these landing tests of the aerial robot with the proposed shock absorbers and landing pads were benchmarked against the conventional landing gears with a rigid structure. The test results revealed that the aerial robot with the 3D printed soft shock absorbers is capable of adapting to varied surface structures and vertical speeds up to $2m/s$ without deterioration of performance. The total impact force that can be absorbed by the novel landing mechanism is up to $540N$.

This work is an example of Aerial Biorobotics which bridges research on aerial robotics control and navigation with biologically inspired mechanical resilience and morphological adaptation, showing innovative solutions to challenges in aerial robotic engineering.

Compared to commercially available simple dampers with a similar size, the proposed Sarrus shock-absorber has a relatively larger stroke, whilst the soft materials used for printing the corrugated shell mechanism provide flexibility of bending for local adaptability to surface structure. Further, the 3D printable shock absorber can be customized and directly 3D printed according to needs of application. A comprehensive modelling with consideration of the additive manufacturing process and various filament materials will lead to better understanding of the design principles for 3D printable functional mechanical systems for aerial robots

Acknowledgments

This work was supported by the Aerial ABM (http://www.aerial-abm.com/), an project from Engineering and Physical Sciences Research Council (EPSRC) UK under grant agreement EP/N018494/1.

References

Altenbach, J. S. (1979). *Locomotor morphology of the vampire bat, Desmodus rotundus*. American Society of Mammalogists.

Bhushan, B. (2009). Biomimetics: lessons from nature–an overview.

Briod, A., Kornatowski, P., Zufferey, J.-C., and Floreano, D. (2014). A collision-resilient flying robot. *Journal of Field Robotics*, 31(4):496–509.

Burroughs, M. L., Freckleton, K. B., Abbott, J. J., and Minor, M. A. (2016). A sarrus-based passive mechanism for rotorcraft perching. *Journal of Mechanisms and Robotics*, 8(1):011010.

Carruthers, A. C., Taylor, G. K., Walker, S. M., and Thomas, A. L. (2007a). Use and function of a leading edge flap on the wings of eagles. *AIAA Paper*, 43:2007.

Carruthers, A. C., Thomas, A. L., and Taylor, G. K. (2007b). Automatic aeroelastic devices in the wings of a steppe eagle aquila nipalensis. *Journal of Experimental Biology*, 210(23):4136–4149.

Culler, E., Thomas, G., and Lee, C. (2012). A perching landing gear for a quadcopter. In *53rd AIAA/ASME/ASCE/AHS/ASC Structures, Structural Dynamics and Materials Conference*, page 1722.

Dai, J. S. and Cannella, F. (2008). Stiffness characteristics of carton folds for packaging. *Journal of mechanical design*, 130(2):022305.

Daler, L., Lecoeur, J., Hählen, P. B., and Floreano, D. (2013). A flying robot with adaptive morphology for multi-modal locomotion. In *Intelligent Robots and Systems (IROS), 2013 IEEE/RSJ International Conference on*, pages 1361–1366. IEEE.

Dickson, J. D. and Clark, J. E. (2013). Design of a multimodal climbing and gliding robotic platform. *IEEE/ASME Transactions On Mechatronics*, 18(2):494–505.

Dollar, A. M., Cho, K.-J., Fearing, R. S., and Park, Y.-L. (2015). Special issue: Fabrication of fully integrated robotic mechanisms. *Journal of Mechanisms and Robotics*, 7(2):020201.

Doyle, C. E., Bird, J. J., Isom, T. A., Kallman, J. C., Bareiss, D. F., Dunlop, D. J., King, R. J., Abbott, J. J., and Minor, M. A. (2013). An avian-inspired passive mechanism for quadrotor perching. *IEEE/ASME Transactions on Mechatronics*, 18(2):506–517.

Estrada, M. A., Hawkes, E. W., Christensen, D. L., and Cutkosky, M. R. (2014). Perching and vertical climbing: Design of a multimodal robot. In *Robotics and Automation (ICRA), 2014 IEEE International Conference on*, pages 4215–4221. IEEE.

Evangelista, C., Kraft, P., Dacke, M., Reinhard, J., and Srinivasan, M. V. (2010). The moment before touchdown: landing manoeuvres of the honeybee apis mellifera. *Journal of Experimental Biology*, 213(2):262–270.

Floreano, D. and Wood, R. J. (2015). Science, technology and the future of small autonomous drones. *Nature*, 521(7553):460.

Greenberg, H., Gong, M., Magleby, S., and Howell, L. (2011). Identifying links between origami and compliant mechanisms. *Mechanical Sciences*, 2(2):217–225.

Kalantari, A. and Spenko, M. (2014). Modeling and performance assessment of the hytaq, a hybrid terrestrial/aerial quadrotor. *IEEE Transactions on Robotics*, 30(5):1278–1285.

Kovač, M. (2014). The bioinspiration design paradigm: A perspective for soft robotics. *Soft Robotics*, 1(1):28–37.

Kovač, M. (2016). Learning from nature how to land aerial robots. *Science*, 352(6288):895–896.

Kovač, M., Schlegel, M., Zufferey, J.-C., and Floreano, D. (2010). Steerable miniature jumping robot. *Autonomous Robots*, 28(3):295–306.

Kuribayashi, K., Tsuchiya, K., You, Z., Tomus, D., Umemoto, M., Ito, T., and Sasaki, M. (2006). Self-deployable origami stent grafts as a biomedical application of ni-rich tini shape memory alloy foil. *Materials Science and Engineering: A*, 419(1):131–137.

Leutenegger, S., Lynen, S., Bosse, M., Siegwart, R., and Furgale, P. (2014). Keyframe-based visual–inertial odometry using nonlinear optimization. *The International Journal of Robotics Research*, page 0278364914554813.

Li, S., Vogt, D. M., Rus, D., and Wood, R. J. (2017). Fluid-driven origami-inspired artificial muscles. *Proceedings of the National Academy of Sciences*, 114(50):13132–13137.

Liu, H., Ravi, S., Kolomenskiy, D., and Tanaka, H. (2016). Biomechanics and biomimetics in insect-inspired flight systems. *Phil. Trans. R. Soc. B*, 371(1704):20150390.

Low, K., Hu, T., Mohammed, S., Tangorra, J., and Kovac, M. (2015). Perspectives on biologically inspired hybrid and multi-modal locomotion. *Bioinspiration & biomimetics*, 10(2):020301.

Luo, C., Li, X., Li, Y., and Dai, Q. (2016). Biomimetic design for unmanned aerial vehicle safe landing in hazardous terrain. *IEEE/ASME Transactions on Mechatronics*, 21(1):531–541.

Ma, J., Hou, D., Chen, Y., and You, Z. (2016). Quasi-static axial crushing of thin-walled tubes with a kite-shape rigid origami pattern: Numerical simulation. *Thin-Walled Structures*, 100:38–47.

Ma, J. and You, Z. (2014). Energy absorption of thin-walled square tubes with a prefolded origami pattern—part i: geometry and numerical simulation. *Journal of Applied Mechanics*, 81(1):011003.

MacCurdy, R., Katzschmann, R., Kim, Y., and Rus, D. (2016a). Printable hydraulics: a method for fabricating robots by 3d co-printing solids and liquids. In *Robotics and Automation (ICRA), 2016 IEEE International Conference On*, pages 3878–3885. IEEE.

MacCurdy, R., Lipton, J., Li, S., and Rus, D. (2016b). Printable programmable viscoelastic materials for robots. In *Intelligent Robots and Systems (IROS), 2016 IEEE/RSJ International Conference on*, pages 2628–2635. IEEE.

Manzanera, R. J. and Smith, S. (2015). Flight in nature ii: How animal flyers land. *The Aeronautical Journal*, 119(1213):281–299.

Markforged Materials (2016). URL: https://markforged.com/materials/.

MATRICE 100 quadcopter for developers (2015). URL: https://www.dji.com/matrice100/features.

Mur-Artal, R. and Tardós, J. D. (2017). Orb-slam2: An open-source slam system for monocular, stereo, and rgb-d cameras. *IEEE Transactions on Robotics*.

Norman, A., Seffen, K., and Guest, S. (2009). Morphing of curved corrugated shells. *International Journal of Solids and Structures*, 46(7):1624–1633.

Pope, M. T., Kimes, C. W., Jiang, H., Hawkes, E. W., Estrada, M. A., Kerst, C. F., Roderick, W. R., Han, A. K., Christensen, D. L., and Cutkosky, M. R. (2017). A multimodal robot for perching and climbing on vertical outdoor surfaces. *IEEE Transactions on Robotics*, 33(1):38–48.

Roderick, W. R., Cutkosky, M. R., and Lentink, D. (2017). Touchdown to take-off: at the interface of flight and surface locomotion. *Interface focus*, 7(1):20160094.

Salerno, M., Zhang, K., Menciassi, A., and Dai, J. S. (2016). A novel 4-dof origami grasper with an sma-actuation system for minimally invasive surgery. *IEEE Transactions on Robotics*, 32(3):484–498.

Seffen, K. A. (2012). Compliant shell mechanisms. *Phil. Trans. R. Soc. A*, 370(1965):2010–2026.

Song, J., Chen, Y., and Lu, G. (2012). Axial crushing of thin-walled structures with origami patterns. *Thin-Walled Structures*, 54:65–71.

Tieu, M., Michael, D. M., Pflueger, J. B., Sethi, M. S., Shimazu, K. N., Anthony, T. M., and Lee, C. L. (2016). Demonstrations of bio-inspired perching landing gear for uavs. In *Bioinspiration, Biomimetics, and Bioreplication 2016*, volume 9797, page 97970X. International Society for Optics and Photonics.

Tolman, S. S., Delimont, I. L., Howell, L. L., and Fullwood, D. T. (2014). Material selection for elastic energy absorption in origami-inspired compliant corrugations. *Smart Materials and Structures*, 23(9):094010.

Ultimaker TPU 95A (2017). URL: https://ultimaker.com/en/products/materials/tpu-95a.

Vidyasagar, A., Zufferey, J.-C., Floreano, D., and Kovač, M. (2015). Performance analysis of jump-gliding locomotion for miniature robotics. *Bioinspiration & biomimetics*, 10(2):025006.

Zhang, K., Qiu, C., and Dai, J. S. (2015). Helical kirigami-enabled centimeter-scale worm robot with shape-memory-alloy linear actuators. *Journal of Mechanisms and Robotics*, 7(2):021014.

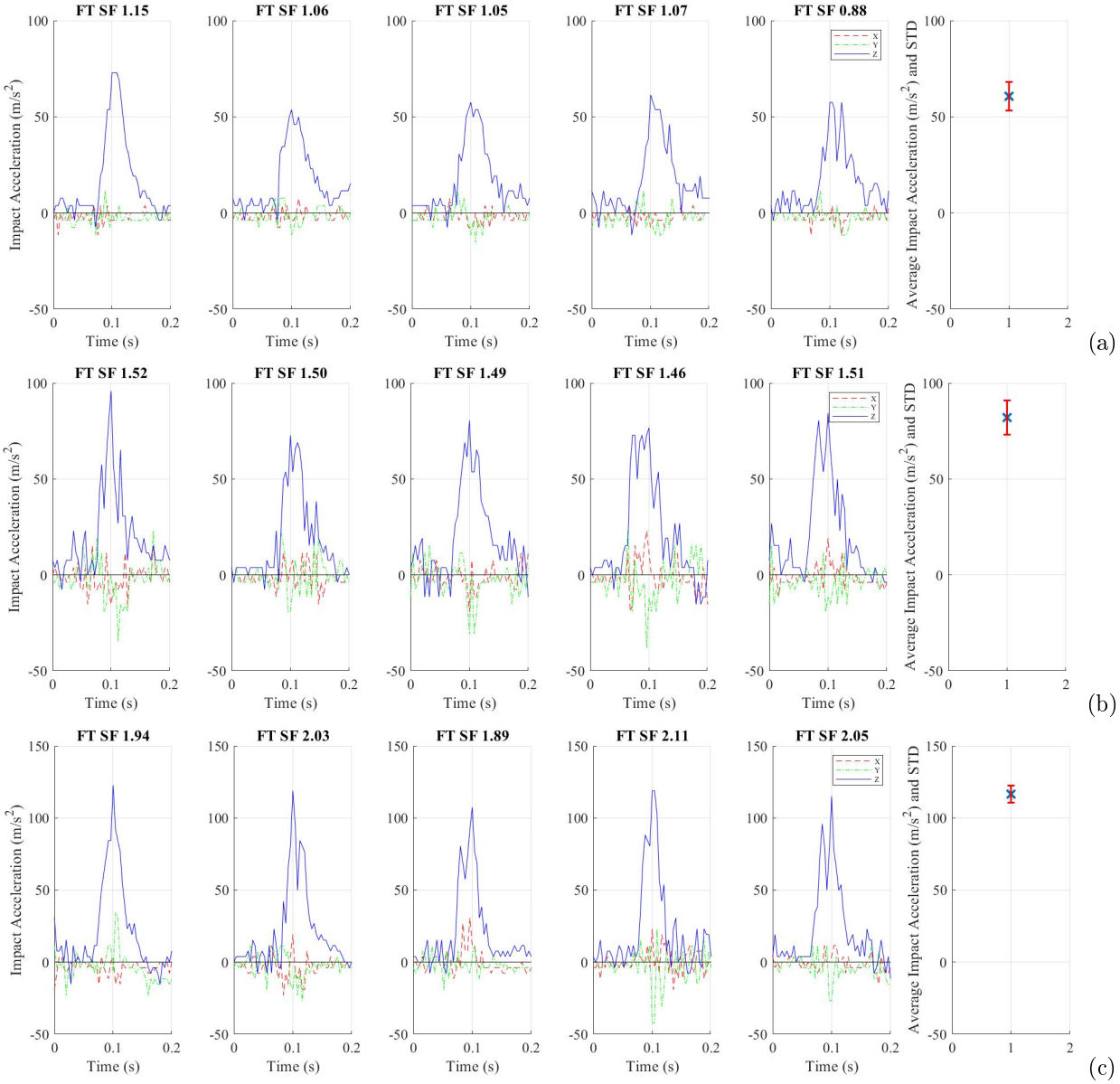

Figure 17: Landing tests on static horizontal flat surface structure: peak, average and standard deviations of impact accelerations of five tests with average vertical landing speed at (a) $1.042 m/s$, (b) $1.496 m/s$ and (c) $2.058 m/s$. (FT: Flat surface, SF: Soft leg).

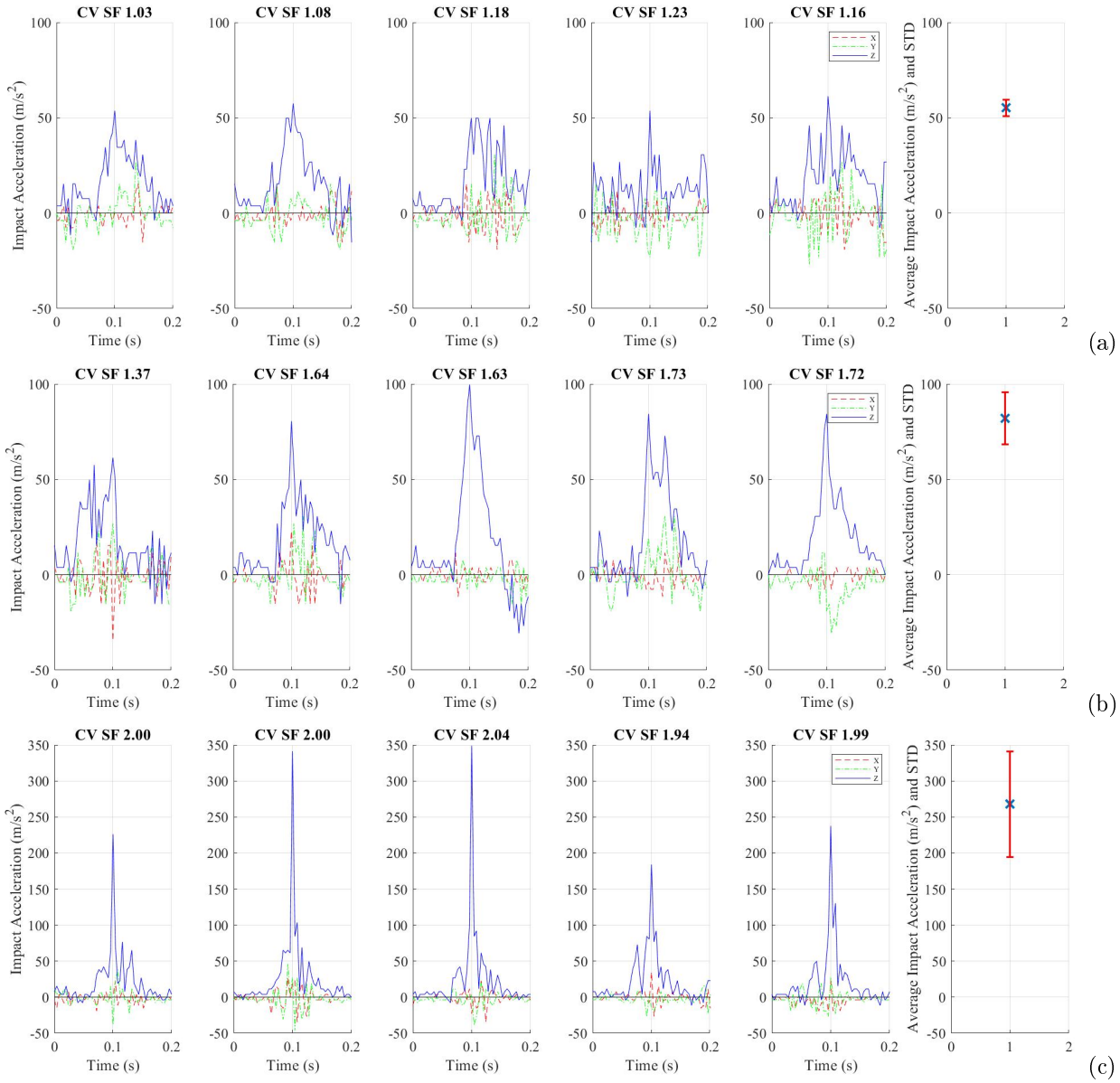

Figure 19: Impact acceleration of landing tests on static convex surface structure: peak, average and standard deviations of impact accelerations of five tests with average vertical landing speeds at (a) $1.136m/s$, (b) $1.618m/s$ and (c) $1.994m/s$. (CV: Convex surface, SF: Soft leg)

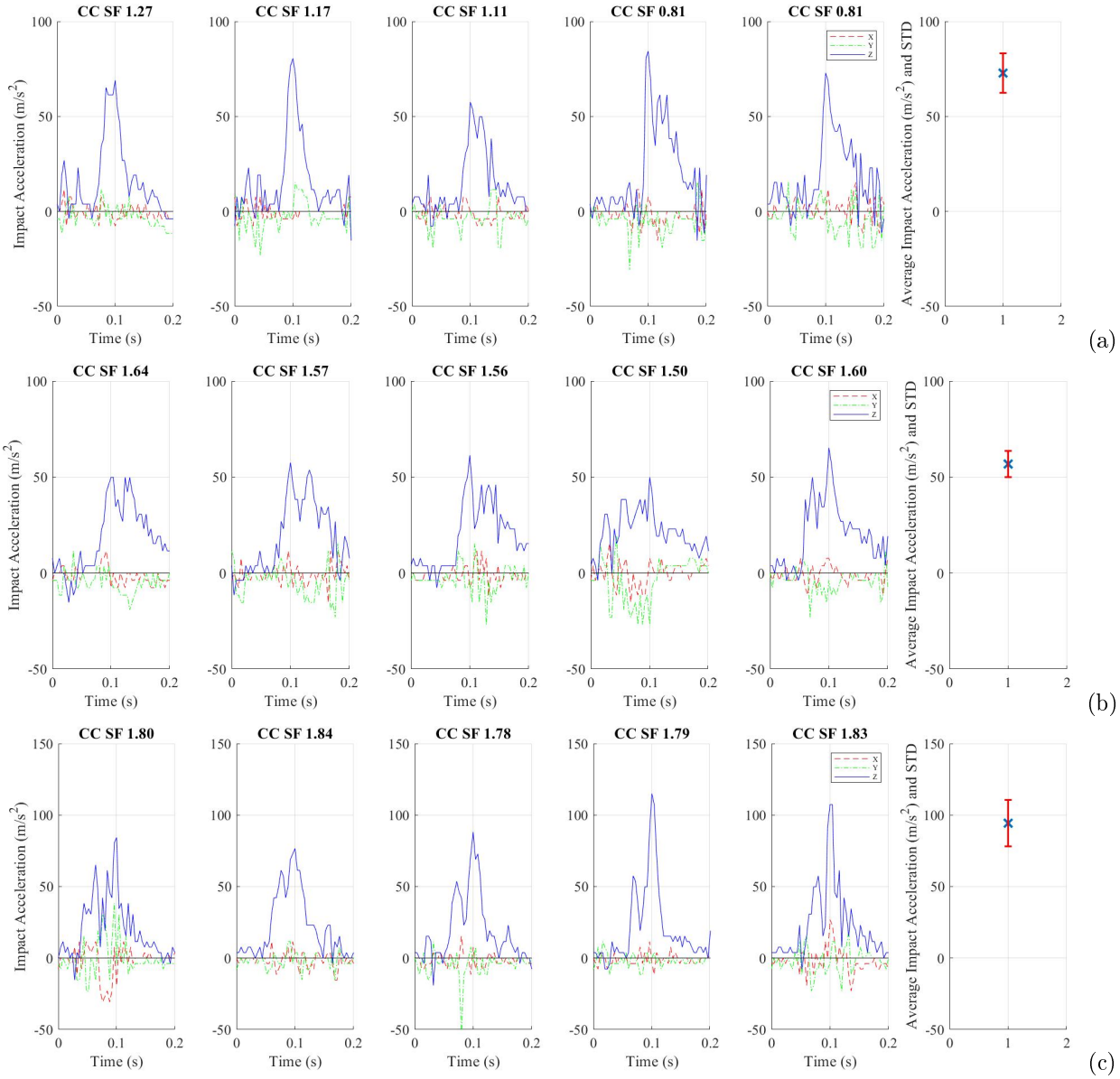

Figure 21: Impact acceleration of landing tests on static concave surface structure: peak, average and standard deviations of impact accelerations of five tests with average vertical landing speeds at (a) $1.034m/s$, (b) $1.574m/s$ and (c) $1.808m/s$. (CC: Concave surface, SF: Soft leg)

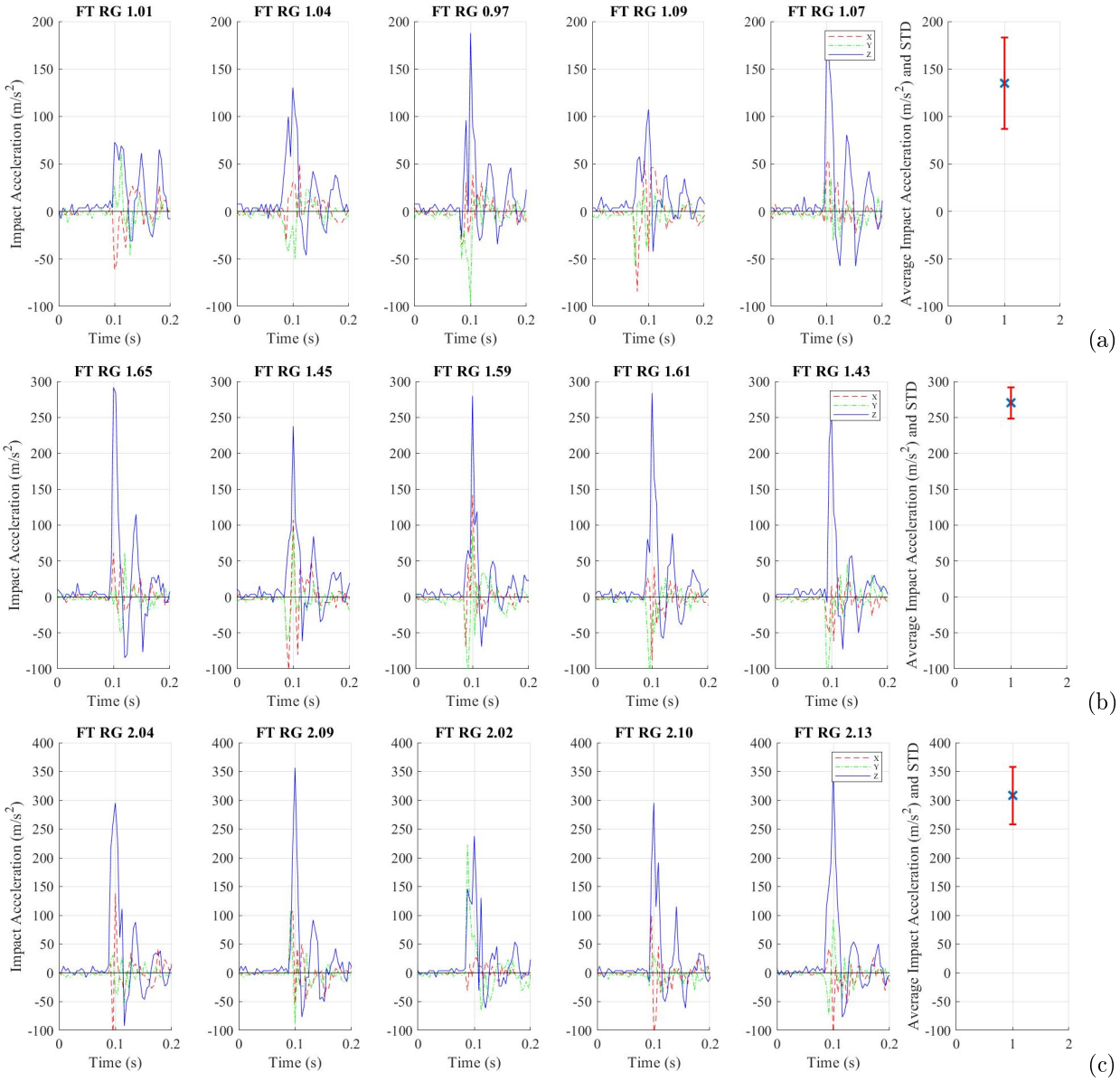

Figure 22: Impact acceleration of landing tests on static flat steel plate: peak, average and standard deviations of impact accelerations of five tests with average vertical landing speeds at (a) $1.036m/s$, (b) $1.546m/s$ and (c) $2.076m/s$. (FT: Flat surface, RG: Rigid legs)

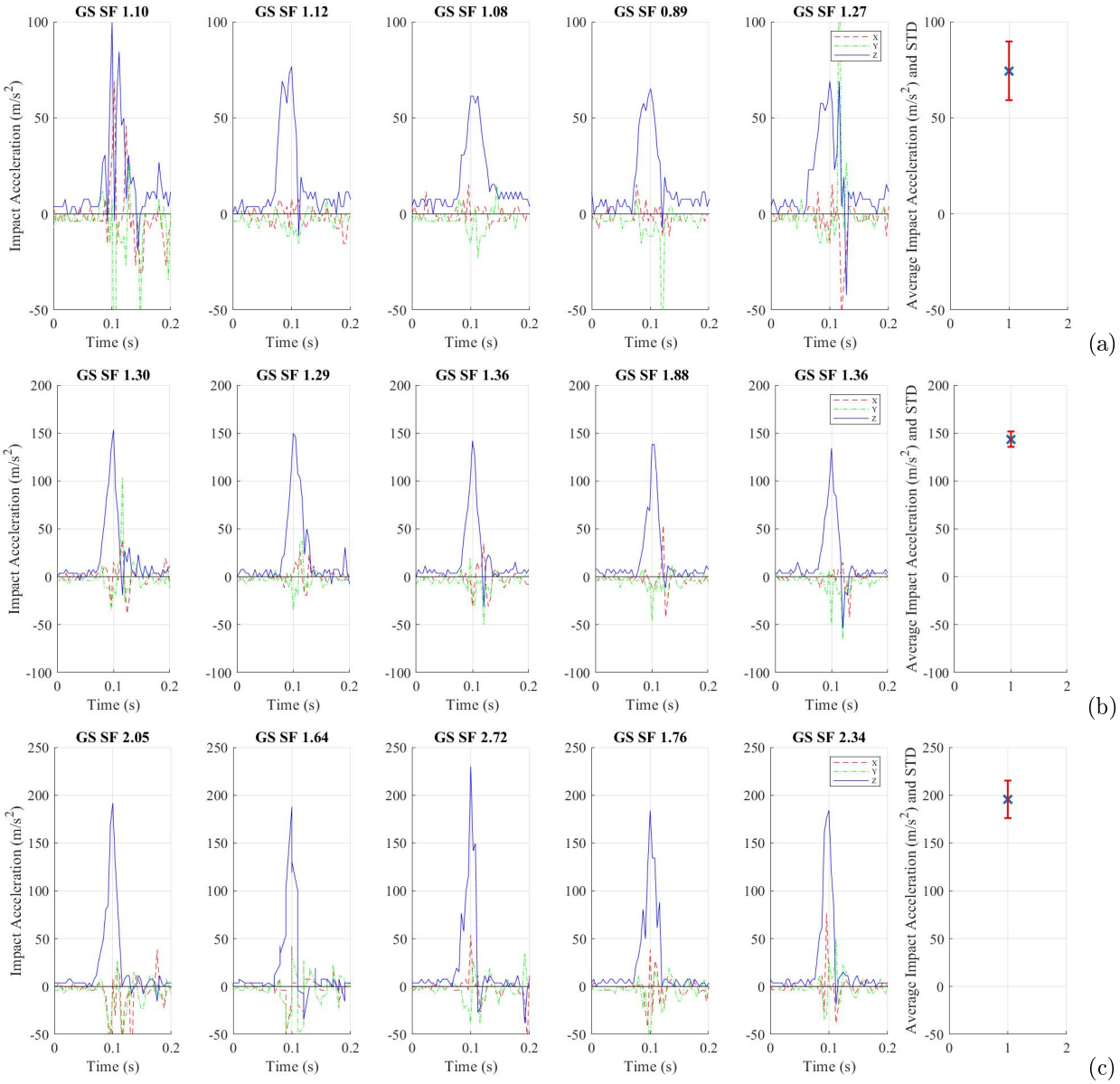

Figure 25: Impact acceleration of landing tests on grassy field: peak, average and standard deviations of impact accelerations of five tests with average vertical landing speed at (a) $1.092 m/s$, (b) $1.438 m/s$ and (c) $2.102 m/s$. (GS: Grassy field, SF: Soft leg)